

1
2 **Water Table and Permeability Estimation from Multi-Channel Seismoelectric**
3 **Spectral Ratios**

4 **Kaiyan Hu^{1,2,4}, Hengxin Ren^{3,4*}, Qinghua Huang^{1*}, Ling Zeng⁴, Karl E. Butler⁵, Damien**
5 **Jougnot⁶, Niklas Linde⁷, Klaus Holliger⁷**

6 ¹Department of Geophysics, School of Earth and Space Sciences, Peking University, Beijing
7 100871, China.

8 ²Shenzhen Institute, Peking University, Shenzhen 518057, China.

9 ³Guangdong Provincial Key Laboratory of Geophysical High-resolution Imaging Technology,
10 Southern University of Science and Technology, Shenzhen 518055, China.

11 ⁴Department of Earth and Space Sciences, Southern University of Science and Technology,
12 Shenzhen 518055, China.

13 ⁵Department of Earth Sciences, University of New Brunswick, P.O. Box 4400, Fredericton, New
14 Brunswick E3B 5A3, Canada.

15 ⁶Sorbonne Université, CNRS, EPHE, UMR 7619 METIS, Paris F-75005, France.

16 ⁷Institute of Earth Sciences, University of Lausanne, CH-1015 Lausanne, Switzerland.

17 Corresponding author: Qinghua Huang (huangq@pku.edu.cn)

18 Hengxin Ren (renhx@sustech.edu.cn)

19 **Key Points:**

- 20
- Multi-channel seismoelectric spectral ratios are sensitive to the water table depth and
21 the permeabilities of shallow layers
 - Broad learning neural network is introduced to perform the inversion efficiently
22
 - This study allows us to monitor the water table depth from the ground surface for an
23 otherwise pre-defined model
24

25 Abstract

26 Recent developments in predicting and interpreting seismoelectric signals suggest a great
27 potential for studying near-surface hydrogeological properties, particularly in the vadose zone.
28 Previous studies have revealed that the seismoelectric spectral ratios obtained from earthquake-
29 triggered seismoelectric data contain valuable hydrogeological information concerning porous
30 media (e.g., permeability, porosity, fluid viscosity, and salinity). This study introduces Multi-
31 Channel SeismoElectric Spectral Ratios (MC-SESRs) by considering an active seismic source
32 acting on the ground surface. The frequency- and saturation-dependent excess charge density is
33 adopted to calculate the cross-coupling coefficients. Applying a supervised learning task based
34 on a flat neural network, the so-called “broad learning” model, to map and extract the features of
35 MC-SESRs data, we seek to determine the permeability and the water table depth. Our results
36 indicate that (1) MC-SESRs are sensitive to the water table depth and permeability; (2) using
37 more traces of SESRs data for inversion can increase accuracy; (3) the changing water table can
38 be rapidly determined by the MC-SESRs by resorting to the broad learning inverse model, and it
39 can attain an excellent accuracy while disturbed by data noise and misspecified model
40 parameters (e.g., porosity and permeability) with errors of up to 20%. The proposed MC-SESRs
41 inversion has potential applications for non-invasive monitoring in shallow porous media (e.g.,
42 frost thawing and geothermal upwelling).

43 Plain Language Summary

44 A seismic source acting on the ground or occurring in porous materials containing water will
45 generate seismic and electromagnetic field waves. The spectral ratios between the electric field
46 and the seismic field are defined as SeismoElectric Spectral Ratios (SESRs), which are sensitive
47 to physical properties’ contrasts at layer boundaries (e.g., water table and hydrogeological and/or
48 lithological layer boundaries). Applying SESRs to reconstruct hydrogeological parameters
49 eliminates the need to know the seismic source function, which greatly facilitates quantitative
50 interpretation. However, SESRs are often acquired by natural earthquakes in previous studies. It
51 limits interpreting SESRs to one-trace data. This study uses an active seismic source to obtain the
52 Multi-Channel SESRs (MC-SESRs). We conduct several experiments on synthetic MC-SESRs
53 data by using a neural network to obtain water table depths and permeabilities for a layered Earth
54 model. Our results show that the trained neural network can instantly predict the time-variant

55 water table depths accurately. This study indicates that the quantitative interpretation of MC-
56 SESRs data allows for effective and rapid characterization of near-surface hydrogeological
57 properties and also provide a possible approach for the non-invasive monitoring of
58 hydrogeological variations in shallow porous media by using controllable source.

59

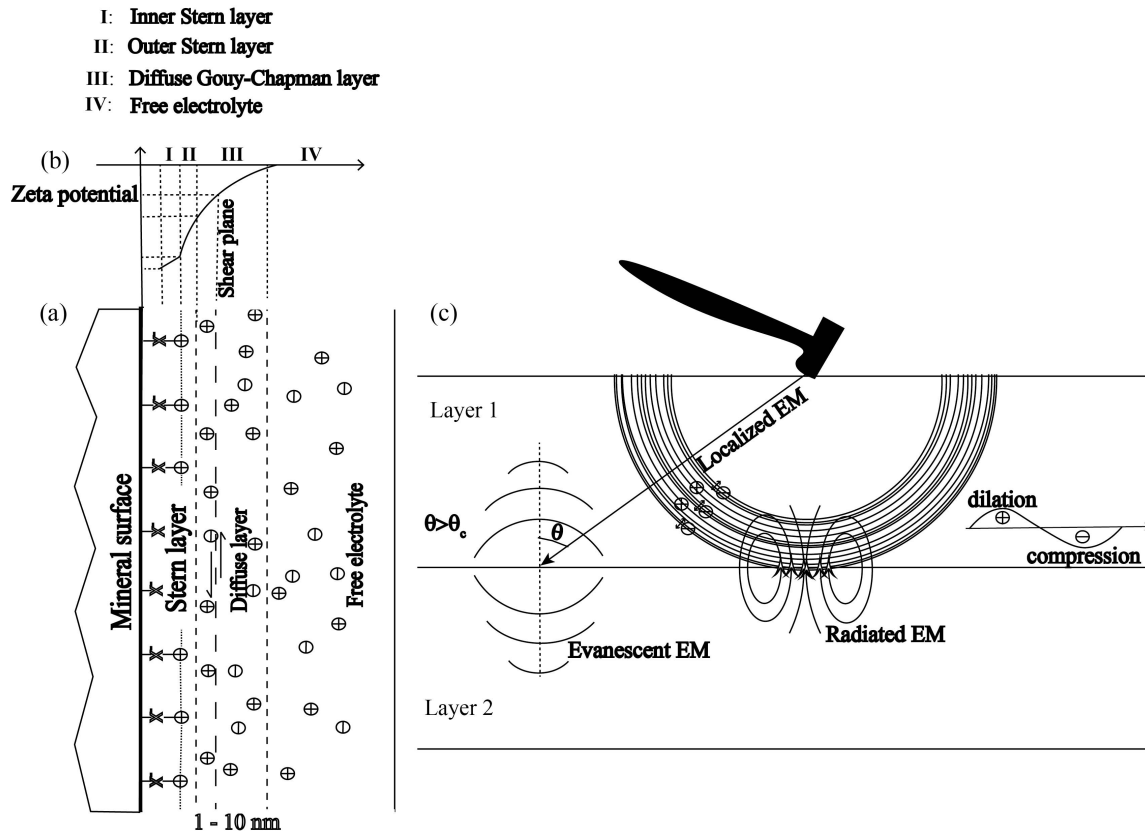
60 **Keywords** Hydrogeophysics; Seismoelectric coupling; Vadose zone; Water table monitoring;
61 Seismoelectric spectral ratios; Broad learning

62 **1. Introduction**

63 In porous media, the surface of the solid grains (e.g., silicate minerals) is typically
64 negatively charged due to fluid-mineral interactions (Glover & Jackson, 2010; Hunter, 1981;
65 Revil et al., 2015). Considering the electrical double layer (EDL) model at the microscopic scale
66 (1 - 10 nm) (Figure 1a), a portion of the counterions (cations for negatively charged mineral
67 surfaces) coats the interface between the mineral surface and pore fluid forming the Stern layer
68 while the remaining excess charges are distributed in the diffuse Gouy-Chapman layer (Glover &
69 Jackson, 2010; Revil & Jardani, 2013). There is a shear plane in the diffuse Gouy-Chapman
70 layer, beyond which the pore fluid and ions can move relative to the solid frame. As shown in
71 Figure 1b, the electrical potential at the shear plane is defined as the Zeta potential (Hunter,
72 1981; Jougnot et al., 2020). The Zeta potential is commonly used to estimate the electrokinetic
73 coupling coefficient, which characterizes the relationship between electrical and hydraulic
74 potential differences associated with fluid flow within a porous medium (Hunter, 1981). Note
75 that all acronyms used in this paper are listed in Table A1 of Appendix A.

76 Relative motions occur during the passage of seismic wavefields. Due to the
77 electrokinetic effect, this process may generate streaming currents and natural electric fields
78 (Pride, 1994; Revil et al., 2015; Revil & Linde, 2006). This process is commonly called
79 seismoelectric (SE) conversion. The SE signals contain valuable information concerning the
80 physical properties of both the pore fluid and the solid skeleton. The SE method can be used to
81 determine hydrogeological properties provided the data measured on the ground surface or in
82 boreholes are properly interpreted (Revil et al., 2012). During the past two decades, the SE
83 method has seen significant development through (1) theoretical studies (e.g., Huang, 2002;
84 Jougnot & Solazzi, 2021; Monachesi et al., 2018; Solazzi et al., 2022; Thanh et al., 2022), (2)

85 numerical modeling approaches (e.g., Garambois & Dietrich, 2002; Grobge & Slob, 2016;
86 Haines & Pride, 2006; Hu & Gao et al., 2011; Jougnot et al., 2013; Ren et al., 2016a, b; Zheng et
87 al., 2021), (3) physical laboratory experiments (e.g., Bordes et al., 2015; Devis et al., 2018;
88 Wang et al., 2020; Zhu & Toksöz, 2013), and (4) field measurements (e.g., Butler et al., 2018;
89 Dupuis & Butler, 2006; Garambois & Dietrich, 2001; Rabbel et al., 2020; Thompson & Gist,
90 1993). As the understanding of SE signals grows, this method is of increasing interest to
91 researchers in near-surface geophysics (e.g., Grobge et al., 2020). The electromagnetic (EM)
92 wave fields originating from seismic excitations are regarded as a superposition of three types of
93 patterns (Figure 1c): (1) localized SE field waves accompanying seismic waves in porous media,
94 which are also commonly referred to as coseismic electric field waves (Bordes et al., 2015;
95 Jougnot et al., 2013; Pride & Garambois, 2002); (2) radiation waves induced on interfaces or
96 directly converted from a seismic source (Dupuis et al., 2007; Haartsen & Pride, 1997;
97 Garambois & Dietrich, 2002; Pride & Haartsen, 1996) and (3) evanescent waves generated on
98 interfaces if the seismic incident angle is larger than the critical angle (Butler et al., 2018;
99 Dzieran et al., 2019; Ren et al., 2016a; Yuan et al., 2021; Zheng et al., 2021). The generation of
100 interfacial radiation and evanescent SE waves results from property contrasts at an interface
101 (Garambois & Dietrich, 2002; Ren et al. 2016a, b). Interfacial radiation SE waves and
102 evanescent SE waves offer a way to examine permeability or porosity contrasts (Dzieran et al.,
103 2019, 2020), parameters determining the soil moisture characteristic (Zyserman et al., 2017),
104 strong saturation contrasts such as the water table (Bordes et al., 2015; Warden et al., 2013), and
105 other parameters (e.g., Archie's parameters, density, bulk, and shear modulus).



106

107 **Figure 1.** Schematic illustration of the generation of electromagnetic waves by seismoelectric
 108 conversion. (a) and (b) Electrical double layer and the corresponding electrical potential
 109 distribution. (c) Generation of localized, interfacial radiated, and evanescent electromagnetic
 110 wavefields due to an active seismic source.

111 Based on numerical simulation studies, Ren et al. (2016b) put forward the idea that
 112 evanescent SE waves could be the main contribution to EM signals observed during earthquakes.
 113 This idea was later adopted by Dzieran et al. (2019) to investigate earthquake-triggered SE
 114 signals in data from Northern Chile. They show that the SeismoElectric Spectral Ratios (SESRs),
 115 defined as the ratios between the absolute values of the electric field and the seismic acceleration
 116 in the frequency domain, have a site-specific frequency dependence with a decreasing amplitude
 117 with increasing frequency. Dzieran et al. (2019) explain this trend by the fact that the amplitudes
 118 of evanescent SE waves decay approximately with $\exp(-\omega p \Delta z)$, where ω is the angular
 119 frequency, p is the EM wave slowness, and Δz is the separation in depth between the receiver
 120 and the interface (Ren et al. 2018). Dzieran et al. (2019, 2020) successfully apply the SESRs to
 121 interpret shallow layered porous media's porosity and fluid salinity. However, Dzieran et al.

122 (2020) state that the SESRs are less sensitive to permeability variations. Inspired by Dzieran et
123 al. (2019, 2020), this study extends the applications of SESRs data in several ways.

124 First, we change the strategy of calculating the SE coupling coefficient. Dzieran et al.
125 (2019, 2020) calculate the electrokinetic coupling coefficient defined by Pride (1994),
126 accounting for the Zeta potential. Instead, we rely on the effective excess charge density to
127 calculate the electrokinetic coupling coefficient (e.g., Revil & Mahardika, 2013; Revil et al.,
128 2015). Both in saturated and partially-saturated conditions, the effective excess charge density is
129 highly correlated with permeability (Guarracino & Jougnot, 2018; Jougnot et al., 2020; Soldi et
130 al., 2019). At low frequencies, the ratio of the effective excess charge density at partial water
131 saturation to the excess charge density at full saturation is proportional to the reciprocal of water
132 saturation under the assumption of a thick EDL model (Linde et al., 2007a; Revil et al., 2007).
133 To account for frequency dependence, we adopt an approximate empirical formulation by using
134 the relaxation time to relate the quasi-static to dynamic electrokinetic coupling coefficient
135 proposed by Revil & Mahardika (2013), which has been tested by experimental measurements
136 and other approaches (Jougnot & Solazzi, 2021).

137 Second, we consider the case of having both the seismic source and sensors located near
138 the ground surface, which is very common in active-source SE field measurements (e.g., Butler
139 et al., 1996, 2018; Dupuis et al., 2007; Garambois & Dietrich, 2001; Mikhailov et al., 1997;
140 Thompson & Gist, 1993). Three-dimensional SE forward modeling algorithms using the
141 reflectivity method (e.g., Garambois & Dietrich, 2002; Grobbe & Slob, 2016; Haartsen & Pride,
142 1997; Ren et al., 2007, 2010) to calculate full waveform simulations for layered media suffer
143 from highly time-consuming computations when the source and receivers both lie very close to
144 surface. As the computation of full waveforms relies on numerical integration in the
145 wavenumber domain, the integrand oscillates strongly with the wavenumber when the depth
146 difference between the source and the receiver is small, which may cause a slow convergence.
147 Zheng et al. (2021) solved this convergence problem by adopting the peak-trough averaging
148 method (Zhang et al., 2001, 2003), which selects peak and trough values in a stably oscillating
149 sequence to apply the repeated average method (Dahlquist & Björck, 1974). Hence it offers an
150 accurate and efficient tool for active-source SE forward modeling. This allows us to deal with
151 any source-receiver geometries, particularly ground-based seismic sources. The Amplitude
152 Variation versus Offset (AVO) method based on multi-channel observation has been widely

153 applied in oil and gas exploration (Rutherford & Williams, 1989). Multi-channel measurements
154 can also be implemented in SE field experiments for stratified sediments. For example, Butler et
155 al. (2018) presented that the multi-channel high-resolution EM field data, illustrating multiple
156 modes of SE signals, providing information on subsurface porous materials complementary to
157 that provided by multi-channel seismic reflection data. Moreover, Rabbel et al. (2020) document
158 the potential of using the interfacial SE responses to map the water table by comparing the multi-
159 channel SE measurements with other geophysical measurements, such as ground-penetrating
160 radar and traditional seismic recordings. Inspired by AVO and SESRs, we propose a Multi-
161 Channel SESRs (MC-SESRs) method that, in addition to frequency variations, makes use of the
162 variations of SESRs with respect to the source-receiver offsets. Thus, we can use more spatial
163 information of SESRs data in the inversions and obtain an improved reconstruction accuracy.

164 Third, the SESRs are determined by different parameters in different complicated non-
165 linear ways. For example, the water table variations affect the water saturation distribution,
166 which determines the effective permeability (e.g., Mualem, 1976; van Genuchten, 1980), the
167 permittivity (e.g., Linde et al., 2006), the electrical conductivity, the electrokinetic coupling
168 coefficient (e.g., Warden et al., 2013; Revil & Mahardika, 2013; Zyserman et al., 2017), the bulk
169 density, the elastic moduli, the seismic velocity (e.g., Mao et al., 2022; Solazzi et al., 2021) and
170 so on. Dzieran et al. (2019) mentioned that inverse modeling of SESRs may need a more
171 advanced approach compared to the conventional linearized inversion algorithm used in their
172 work. Machine learning, which is enjoying increasing interest in geophysics, may offer a
173 corresponding option.

174 In this study, we rely on the broad learning (BL) model to invert hydrological parameters
175 using MC-SESRs data. The BL system proposed by Chen and Liu (2017) is a flat neural network
176 with a single lateral layer neural network, in contrast to deep structured neural networks. It is
177 developed from the Random Vector Functional Link Neural Network (RVFLNN) (Pao et al.,
178 1994) to apply an enhancement layer to link the input and output. Broadly expanding the
179 enhancement nodes may enhance the capacity to approach non-linear problems. It only needs to
180 learn the matrix weights of the link between the enhancement layer and output. Other matrix
181 weights are randomly generated. Thus, the RVFLNN is a flat net without hidden layers, which
182 avoids overtraining the neural network with many adjustable hyperparameters (Pao et al., 1994).
183 Correspondingly, the BL structure improves the RVFLNN by adding a mapping feature layer to

184 replace the original input based on the sparse autoencoder. Hence the BL structure first captures
185 the features of input data in the mapping feature layer. Since the BL network structure is fixed,
186 its main advantage is that it avoids elusive complicated deep architectures and iterative training
187 processes (Gong et al., 2022). Its efficient capacities for processing noisy time series and text
188 classifications have been verified (Chen & Liu, 2017; Du et al., 2020; Feng et al., 2019; Gong et
189 al., 2022).

190 Most recently, Yang et al. (2022, 2023) applied the BL neural network to Rayleigh wave
191 inversion. Considering a 1-D Earth model, Yang et al. (2022) examined the thickness and shear-
192 wave velocity ranges of each layer by the well-trained BL neural network. Then they used the
193 optimal ranges as the search space of a Bayesian approach to complement the parameter
194 optimization. Their results indicated that this two-stage approach can provide more accurate
195 shear-wave velocity models than without using a priori search space estimated by a BL model.
196 Yang et al. (2023) also verified that using the BL approach to Rayleigh wave inversion may
197 achieve a comparable accuracy but consume less training time than deep convolutional neural
198 networks. In this study, we aim to determine hydrogeological parameters (water table depth and
199 shallow layer permeabilities) under partially-saturated conditions by MC-SESRs data. For a
200 specific investigated area whose layered structure had been determined, the well-trained BL
201 model can, if fed with MC-SESR data, estimate the water table depth and update the
202 permeability in the shallow layer in a quasi-instantaneous manner. Due to its high training
203 efficiency, BL can easily be retrained to optimize the network when more MC-SESRs data is
204 obtained. This study may provide a new monitoring strategy for obtaining the water table depths
205 using the time-lapse MC-SESRs data. It also has the potential application in long-term
206 observations for assessing groundwater storage and monitoring volcanic activities.

207 This paper is structured as follows. Section 2 describes the basic SE coupling equations,
208 numerical simulation of the SE data, and our inversion framework. Section 3 focuses on
209 analyzing the sensitivity of permeability and depth of water table (dwt) to MC-SESRs. Section 4
210 tests the performance of the BL neural network and presents the inversion results. Section 5
211 discusses the inversion results, and we provide conclusions in Section 6.

212 **2. Methodology**213 **2.1. Cross-coupling equations**

214 For fluid-saturated isotropic porous media, the cross-coupled constitutive transport
 215 equations, including macroscopic Ohm's and Darcy's Law, can be expressed in the frequency
 216 domain through the following governing equations (Pride, 1994; Pride & Haartsen, 1996; Revil
 217 & Mahardika, 2013):

$$\mathbf{J} = \sigma^*(\omega)\mathbf{E} + L^*(\omega)(-\nabla p_f + \omega^2 \rho_f \mathbf{u}_s), \quad (1)$$

$$-i\omega \mathbf{w} = L^*(\omega)\mathbf{E} + \frac{k^*(\omega)}{\eta_w}(-\nabla p_f + \omega^2 \rho_f \mathbf{u}_s), \quad (2)$$

$$-p_f = C\nabla \cdot \mathbf{u}_s + M\nabla \cdot \mathbf{w}, \quad (3)$$

$$\mathbf{T} = \left[\left(K_G - \frac{2}{3}G \right) \nabla \cdot \mathbf{u}_s + C\nabla \cdot \mathbf{w} \right] \mathbf{I} + G(\nabla \mathbf{u}_s + \nabla \mathbf{u}_s^T), \quad (4)$$

$$-\rho_b \omega^2 \mathbf{u}_s - \rho_f \omega^2 \mathbf{w} = \left(K_G + \frac{4}{3}G \right) \nabla(\nabla \cdot \mathbf{u}_s) - G\nabla \times \nabla \times \mathbf{u}_s + C\nabla(\nabla \cdot \mathbf{w}) + \mathbf{F}, \quad (5)$$

218 where Equations 1-2 describe the electrokinetic cross-coupling relationship between the electric
 219 field \mathbf{E} (V/m) and the volume-averaged fluid filtration displacement \mathbf{w} (m) = $\phi(\mathbf{u}_f - \mathbf{u}_s)$,
 220 which is defined by the porosity ϕ (m³/m³) and the volume-averaged fluid and solid
 221 displacements (\mathbf{u}_f and \mathbf{u}_s). The subscripts 'f' and 's' designate fluid and solid properties,
 222 respectively. We consider a time-harmonic disturbance varying as $e^{-i\omega t}$ with $i = \sqrt{-1}$ the
 223 imaginary unit, $\omega = 2\pi f$ the angular frequency in rad/s, and f (Hz) the frequency. The
 224 superscript "*" indicates that a property is frequency-dependent and hence complex. $k^*(\omega)$ thus
 225 denotes the frequency-dependent permeability (m²). Permeability reflects the ability of porous
 226 media to allow fluid to flow through the pores. Equations 3 and 4 describe the poroelastic
 227 relations (Biot, 1956, 1962a, b) with \mathbf{I} denoting the identity matrix. The parameters C (Pa) and M
 228 (Pa) are associated with the elastic moduli (Pride, 1994). K_G (Pa) and G (Pa) denote the
 229 undrained bulk modulus and shear modulus of the solid skeleton. ρ_b (kg/m³) and \mathbf{F} (N) in

230 Equation 5 are the mass density of the porous material and the body force applied on the bulk
 231 material, respectively. All parameters and their units used in this study are listed in Table A2 of
 232 Appendix A.

233 Due to harmonic variations of the bulk-stress tensor \mathbf{T} (N/m²) and the pore fluid pressure p_f
 234 (Pa), the flow changes from the viscous laminar regime to the inertial laminar regime beyond the
 235 critical or transition frequency (Revil & Mahardika, 2013; Solazzi et al., 2020, 2022). The
 236 permeability becomes frequency-dependent and complex-valued beyond the critical frequency,
 237 and its absolute value decreases with increasing frequency (Solazzi et al., 2020). η_w denotes the
 238 dynamic viscosity of pore water (1.002×10^{-3} Pa·s). The macroscopic electrical current density
 239 \mathbf{J} (A/m²) is the superposition of the conduction current density $\sigma^*(\omega)\mathbf{E}$ and the streaming current
 240 density \mathbf{J}_{ek}^* written by:

$$\mathbf{J}_{ek}^* = L^*(\omega)(-\nabla p_f + \omega^2 \rho_f \mathbf{u}_s), \quad (6)$$

241 in which $\sigma^*(\omega)$, and $\rho_f = (1 - S_w)\rho_a + \rho_w$ denote the complex electrical conductivity (S/m)
 242 and the fluid density (kg/m³), respectively. S_w , $\rho_a = 1.21$ (kg/m³) and $\rho_w = 1000$ (kg/m³)
 243 are the water saturation, the density of the air and pore water. Note that we consider pore water
 244 as a dilute solution with low salinities (commonly around 0.002 mol/L) and, hence, the solute
 245 density is neglected. For highly saline solutions (e.g., seawater, contaminated water), the mass
 246 density of the solute would need to be included. Unless mentioned otherwise, the parameters
 247 used in this paper refer to standard ambient conditions (1 atm and 20 °C). The presence of
 248 harmonic electric fields usually makes the electrical conductivity of porous materials vary with
 249 frequency due to polarization effects of electrically conductive mineral grains, interfacial
 250 electrochemistry, or colloidal chemistry (Revil, 2013). The effective electrical conductivity in the
 251 frequency domain can be expressed by (Revil et al., 2015):

$$\sigma^*(\omega, S_w) = F^{-1} S_w^n \sigma_w + \sigma_{sur} + i(\sigma_{quad} - \omega \varepsilon_0 \kappa). \quad (7)$$

252 Therein, n denotes the saturation exponent and $F = \phi^{-m}$ is the electrical formation factor in
 253 Archie's first and second laws with cementation exponent m (Archie, 1942). $\varepsilon_0 = 8.85418 \times$

254 10^{-12} F/m is the vacuum permittivity. κ denotes the static effective dielectric constant, which is
 255 the function of the water saturation: (Linde et al., 2006):

$$\kappa(S_w) = \frac{(F-1)\kappa_s + S_w^n \kappa_w + (1-S_w^n)\kappa_a}{F} \quad (8)$$

256 The range of the dielectric constant for most rock-forming minerals is 4-6 and is commonly
 257 assumed to be $\kappa_s = 4$ for dry sand grains in near-surface measurements (e.g., Fitterman, 2015;
 258 Knight & Endres, 2005). $\kappa_w = 80.1$ and $\kappa_a = 1$ represent the dielectric constants of the pore
 259 water and the air, respectively. Based on a volume-averaging method, Equation 8 is derived from
 260 a two-phase model (i.e. pore fluid and solid grains) by Pride (1994), accounting for the effective
 261 pore fluid formed by water and air and combining Archie's first and second laws (Linde et al.,
 262 2006). This equation assumes that the two fluid phases in the pore space are immiscible. The
 263 physical relationship (Equation 8) has been previously used to simulate seismoelectric signals
 264 (e.g., Rosas-Carbajal et al., 2020). The surface electrical conductivity σ_{sur} and the quadrature
 265 electrical conductivity σ_{quad} in Equation 7 are related to the fraction and mobility of counterions
 266 in the diffuse layer and in the Stern layer, respectively (Revil, 2013; Revil et al., 2015). Both
 267 conductivities are functions of water saturation. More details of these coefficients calculated by
 268 material properties and saturation levels, can be found in Table A3 of Appendix A.

269 Based on the EDL model (Figure 1a), Equations 1 and 2 express that the poromechanical
 270 influence contributes to the streaming source current, and the electric field contributes to the
 271 pore-fluid flow under the electroosmosis effect (Revil & Mahardika, 2013). The critical dynamic
 272 parameter $L^*(\omega)$ reflects the cross-coupling relationship. Due to the significance of frequency-
 273 dependent cross-coupling coefficient $L^*(\omega)$ in transport equations, its calculation has attracted
 274 considerable attention in the recent decade (Jougnot & Solazzi, 2021; Jouniaux & Zyserman,
 275 2016; Soldi et al., 2020; Thanh et al., 2022; Warden et al., 2013). A popular approach is using
 276 the Zeta potential to describe the cross-coupling coefficient (Dukhin & Derjaguin, 1974; Pride,
 277 1994; Warden et al., 2013; Zyserman et al., 2017). An alternative is to use the movable
 278 (effective) excess charge density \hat{Q}_v^* (C/m³) and permeability to directly relate the relative flow
 279 to streaming current generation (Revil & Linde, 2006). The cross-coupling coefficient calculated
 280 by both approaches explains some experimental measurements (Bordes et al., 2015; Revil &

281 Mahardika, 2013; Zhu & Toksöz, 2013). In terms of partially-saturated conditions considering
 282 only water and air in the pore space, the latter approach conveniently relates $L^*(\omega)$ to the
 283 effective permeability and \hat{Q}_v^* as functions of the water saturation by (Revil & Mahardika, 2013;
 284 Soldi et al., 2020):

$$L^*(\omega, S_w) = \frac{k^*(\omega, S_w)\hat{Q}_v^*(\omega, S_w)}{\eta_w} \quad (9)$$

285 The frequency-dependent (dynamic) characteristics of permeability and effective excess charge
 286 density are approximately described by the relaxation time or the angular transition frequency
 287 ω_t (rad/s), which determines the transition from the viscous (low frequency) to inertial laminar
 288 flow (high frequency) (Revil & Mahardika, 2013). $\omega_t(S_w)$ is expressed as a function of water
 289 saturation by Revil and Mahardika (2013) and Solazzi et al. (2020):

$$\omega_t = \frac{\eta_w \phi S_w}{\rho_w k_0(S_w) \tau_w(S_w)}, \quad (10)$$

290 where τ_w denotes the tortuosity related to the topology of the pore space. The saturation-
 291 dependent tortuosity is equivalent to $\phi F S_w^{(1-n)}$ based on Archie's law (e.g., Niu & Zhang,
 292 2019; Jougnot et al., 2018; Revil et al., 2007; Revil & Jougnot, 2008). Since $n \geq 1$ ($1 - n \leq 0$),
 293 the tortuosity increases with the decrease of water saturation (e.g., Ghanbarian et al., 2013;
 294 Jougnot et al., 2018), while the transition frequency increases with the decrease of water
 295 saturation. Here, $k_0(S_w)$ denotes the quasi-static ($\omega = 0$) effective permeability as a function of
 296 saturation. When the frequency-dependent effective permeability and excess charge density are
 297 considered, Equation 9 is written by (Revil & Mahardika, 2013):

$$L^*(\omega, S_w) = \frac{k_0(S_w)\hat{Q}_{v,0}(S_w)}{\eta_w \sqrt{1 - \frac{i\omega}{\omega_t}}} \quad (11)$$

298 There are two main approaches to describe this effective excess charge density $\hat{Q}_{v,0}$: either by
 299 volume-averaging (Linde et al., 2007a) or flux-averaging (Jougnot et al., 2012). In this work, the
 300 excess charge density at a saturated state is estimated from permeability using (Jardani et al.,
 301 2007):

$$\log_{10}(\hat{Q}_{v,0}^{\text{sat}}) = -0.82\log_{10}(k_0^{\text{sat}}) - 9.23. \quad (12)$$

302 The superscript ‘sat’ denotes a fully saturated condition. This empirical relationship has been
 303 applied to various samples ranging from different salinities and lithologies even if it did not
 304 consider the effect of salinities of pore water on the excess charge density (Jardani et al., 2007;
 305 Jougnot et al., 2015).

306 Another empirical relationship between the voltage coupling coefficient under saturated
 307 conditions C_0^{sat} (mV/m) and the electrical conductivity of pore water σ_w (S/m) is expressed as
 308 (Linde et al., 2007b):

$$\log(|C_0^{\text{sat}}|) = -0.895 - 1.319 \log(\sigma_w) - 0.1227[\log(\sigma_w)]^2, \quad (13)$$

309 where σ_w is estimated by the salinity C_w (mol/L) (Sen & Goode, 1992):

$$\sigma_w = (5.6 + 0.27T - 1.5 \times 10^{-4}T^2)C_w - \frac{(2.36+0.099T)C_w^{\frac{3}{2}}}{1+0.214C_w}, \quad (14)$$

310 where T is the temperature in Celsius ($^{\circ}\text{C}$). Thus, the voltage coupling coefficient C_0^{sat} varies
 311 with pore water salinity. Compared with laboratory and field measurements, Equation 13 works
 312 well in a range of $10^{-2} - 10^{0.5}$ S/m for σ_w , which covers typical pore water environments (Linde et
 313 al., 2007b, Jougnot et al., 2015; Hu et al., 2020). By changing the unit of C_0^{sat} to V/m, it can be
 314 transformed from the static coupling coefficient L_0^{sat} (A/m²) by:

$$C_0^{\text{sat}} = -\frac{L_0^{\text{sat}}}{\sigma_0}. \quad (15)$$

315 Further, C_0^{sat} can be used to express the $\hat{Q}_{v,0}^{\text{sat}}$ with:

$$\hat{Q}_{v,0}^{\text{sat}} = -\frac{C_0^{\text{sat}}\sigma_0\eta_w}{k_0^{\text{sat}}}. \quad (16)$$

316 We may use Equation 12 to estimate $\hat{Q}_{v,0}^{\text{sat}}$ under a known k_0^{sat} or we may derive $\hat{Q}_{v,0}^{\text{sat}}$ by
 317 Equations 13-16 using the salinity of pore water (Jougnot et al., 2015). Otherwise, C_0^{sat} can be
 318 obtained by measuring the voltage differences and hydraulic pressure differences of samples to
 319 calculate values of $\hat{Q}_{v,0}^{\text{sat}}$ by Equation 16.

320 For partially saturated conditions, we applied the volume-averaging method to scale $\hat{Q}_{v,0}$ by
 321 the effective saturation $S_e = \frac{S_w - S_{\text{wr}}}{1 - S_{\text{wr}}}$ (Linde et al., 2007a; Revil & Cerepi, 2004; Revil et al.,
 322 2007):

$$\hat{Q}_{v,0}(S_w) = \frac{\hat{Q}_{v,0}^{\text{sat}}}{S_e}, \quad (17)$$

323 where S_{wr} (unitless) denotes the residual (irreducible) water saturation. Alternative formulations
 324 have been derived to explicitly describe the dynamic process of $\hat{Q}_{v,0}$ varying with water
 325 saturation based on the characteristic pore-size distribution (Jackson, 2010; Jougnot et al., 2012;
 326 Soldi et al., 2020; Solazzi et al., 2022). Furthermore, the frequency-dependent effective excess
 327 charge density is calculated by applying a scaling factor $\sqrt{1 - \frac{i\omega}{\omega_t}}$ (Revil & Mahardika, 2013),
 328 which also has been further developed by Jougnot and Solazzi (2021) and Thanh et al. (2022).

329 Apart from the effective permeability and excess charge density, other effective
 330 parameters (e.g., the electrical conductivity σ^* , the mass density of fluid ρ_f) in Equations 1 and 2
 331 strongly depends on the water saturation as well. Besides, the two fluid phases in the pore space
 332 affect the mechanical properties (e.g., the effective bulk moduli) that need to be considered in
 333 hydromechanical modeling of the volumetric strain of porous media and the infiltration
 334 displacement (Equations 3-5). This indicates that seismic signals could respond to variations in
 335 water saturation. We summarize the frequency-dependent (dynamic) and saturation-dependent
 336 parameters in Table A3 of Appendix A. More details with regard to the parameters mentioned
 337 above as well as the derived equations can be found in Revil & Mahardika (2013).

338 **2.2. Multi-Channel SeismoElectric Spectral Ratios (MC-SESRs)**

339 For isotropic layered media, as the SE field and the seismic particle acceleration field are
 340 triggered by the same seismic source, the seismic source function can be canceled when we

341 calculate the ratios of SE fields to the seismic acceleration fields in the frequency domain
 342 (Dzieran et al., 2019). Therefore, the SESRs can be represented by the ratio of their Green's
 343 functions $GE(\omega)$ and $Ga(\omega)$, which is expressed as (Dzieran et al., 2019):

$$\text{SESR}(\omega) = \frac{\mathbf{E}(\omega)}{\mathbf{a}(\omega)} = \frac{GE(\omega)}{Ga(\omega)}, \quad (18)$$

344 where $\mathbf{E}(\omega)$ denotes the SE field spectra. $\mathbf{a}(\omega)$ denotes the seismic ground acceleration field
 345 spectra, which also can be replaced by the components of seismic ground velocity spectra with
 346 $i\omega\mathbf{v}(\omega)$ or displacement spectra with $-\omega^2\mathbf{u}(\omega)$. The SESR indicates the ratio of Green's
 347 functions, which contains the information of stratified porous media. The modulus of SESRs
 348 varies with position, or offset from the seismic source, represented by:

$$\text{MC-SESR}(\omega, x_i) = \frac{|E_{x,i}(\omega)|}{|a_{x,i}(\omega)|}, \quad i = 1, 2, \dots, B \quad (19)$$

349 where i denotes the measured points and B is the total number of measured points. Here, $E_{x,i}$ and
 350 $a_{x,i}$ denotes the horizontal electric field and seismic ground acceleration in the frequency domain
 351 at point i .

352 **2.3. Inversion framework**

353 Deterministic inverse modeling (e.g., Gauss-Newton, Conjugate Gradient, Levenberg-
 354 Marquardt) algorithms need to construct an objective function, including the data misfit and a
 355 regularization term. The latter depends on prior and empirical information. In weakly non-linear
 356 problems, the iterative adjustment of model parameters using gradient-based information enables
 357 a minimum objective function to be attained. However, it is time-consuming when we deal with
 358 high-dimension parameter estimation, and these parameters affect the SESRs in a non-linear way.
 359 Furthermore, such deterministic inversions might fail to recover the true model, although the
 360 modeling data well match the observed data (Wu et al., 2021).

361 In this study, we aim to reconstruct the permeability and water table depth using the near-
 362 surface MC-SESRs data. As the water table is affected by land-management practices,
 363 precipitation, evapotranspiration, and other environmental changes, its depth may change with

364 time. Machine learning techniques may allow us to efficiently monitor the dynamic water table.
365 A large number of samples are employed to train a neural network, which can construct the
366 mapping process between the input data (MC-SESRs) and the output data (water table depth and
367 permeability). Once the neural network is well trained, we can adapt it to a specific region to
368 monitor variations of its water table and permeability efficiently. Deep-structured neural
369 networks have been employed in solving geophysical inverse problems (e.g., Laloy et al., 2021;
370 Wu et al., 2021), which are alternatives for the SESRs inversion. But the many hidden layers
371 included in such networks produce a large quantity of hyperparameters, which need large data
372 sets and many training epochs to be estimated. Complicated deep architectures empower the
373 neural network to project a more complex relationship between the input and output layers.
374 However, the computing time is increased due to the iterations of training epochs, and
375 overtrained networks could result. Chen and Liu (2017) propose a broad learning (BL) neural
376 network that adopts a flat architecture without a complex multilayer structure. Its network
377 structure does not change within the training process (Figure 2). It avoids adjusting elusive
378 hyperparameters in the network, and its design largely decreases the training time compared with
379 deep networks. Broadly expanding the mapping layer enhances the capacity of the neural
380 network to approach complicated projecting relationships. More important, the broadly
381 expanding structure can be used for incremental learning without retraining the network when
382 additional data are available in input data (Chen & Liu, 2017). Compared with the performance
383 of deep structured neural networks (e.g., deep convolutional neural networks, deep Boltzmann
384 machines, and deep belief networks) on MNIST and NORB data sets, Chen and Liu (2017)
385 demonstrated that the BL system can ensure a comparable classification accuracy while vastly
386 reducing the training time. Recently, the BL approach has been applied to effectively and
387 efficiently process classification and regression problems (Gong et al., 2022). Therefore, the BL
388 approach is considered here to perform water table depth and permeability inversions using MC-
389 SESRs data.

390 As a supervised machine learning task, we need to generate a large number of training
391 samples. We assume the number of samples is N for training the network and the number of
392 inverted layers of permeability is L . If there are A frequencies and B measured points (traces) in
393 Equation 19, the input matrix \mathbf{X} is MC-SESRs data (Figure 2a). The output matrix \mathbf{Y} is made up
394 of N depths of the water table written by a vector $\mathbf{dwt}_{N \times 1}$ and $N \times L$ permeability matrix written

395 by $\mathbf{K}_{N \times L}$ (Figure 2c). Using the neural-network architecture of the BL model (Chen & Liu,
396 2017), we first need to extract the features of MC-SESRs data as the input layer (Figure 2b):

$$\mathbf{F}_i = \varphi_i(\mathbf{X}\mathbf{W}_i + \boldsymbol{\beta}_i), i = 1, 2, \dots, Q \quad (20)$$

397 where \mathbf{F}_i denotes the i th mapped feature matrix. \mathbf{W}_i and $\boldsymbol{\beta}_i$ denote the random weighting matrix
398 and bias term, which are initially generated by standard uniform distributions in a range of $[-1,1]$.
399 Assuming $A \times B = C$, the sizes of matrices of \mathbf{W}_i and $\boldsymbol{\beta}_i$ are $C \times P$ and $N \times P$, respectively. As
400 shown in Figure 2b, P is the number of feature nodes in each mapping feature group i . Q is the
401 number of mapping features. The function φ_i maps the sum of matrices $\mathbf{X}\mathbf{W}_i + \boldsymbol{\beta}_i$ to $[-1,1]$ by
402 normalizing the minimum and maximum value each row (1,2, ..., N). The sparse autoencoder is
403 employed to shrink the input data and extract its mapping features by adapting \mathbf{W}_i (Chen & Liu,
404 2017). As shown in Equation 20, this feature extracting step of the input data can be replaced by
405 other extracting approaches from popular artificial neural networks (e.g., deep convolutional
406 neural networks) (Gong et al., 2022).

407 The features of input data extracted by mapping feature groups $\mathbf{F}^Q = [\mathbf{F}_1, \mathbf{F}_2, \dots, \mathbf{F}_Q]$ are
408 broadly expanded by M enhancement nodes with:

$$\mathbf{E}_j = \xi_j([\mathbf{F}_1, \mathbf{F}_2, \dots, \mathbf{F}_Q]\mathbf{W}_{ej} + \boldsymbol{\beta}_{ej}), j = 1, 2, \dots, M \quad (21)$$

409 where \mathbf{E}_j denotes the matrix of j th enhancement node. \mathbf{W}_{ej} and $\boldsymbol{\beta}_{ej}$ are randomly generated
410 similar to Equation 20. In this study, we used the hyperbolic tangent sigmoid transfer function as
411 the non-linear activation function $\xi_j(\cdot)$. Each enhancement node is integrated to an enhancement
412 layer with $\mathbf{E}^M = [\mathbf{E}_1, \mathbf{E}_2, \dots, \mathbf{E}_M]$.

413 The output-layer hydrogeological parameters $\mathbf{Y} = [\mathbf{dwt}, \mathbf{K}]$ and the last layer integrated
414 by input features and the enhancement layer are connected by a weighting matrix \mathbf{W}^M :

$$\mathbf{Y} = [\mathbf{F}_1, \mathbf{F}_2, \dots, \mathbf{F}_Q | \mathbf{E}_1, \mathbf{E}_2, \dots, \mathbf{E}_M]\mathbf{W}^M, \quad (22)$$

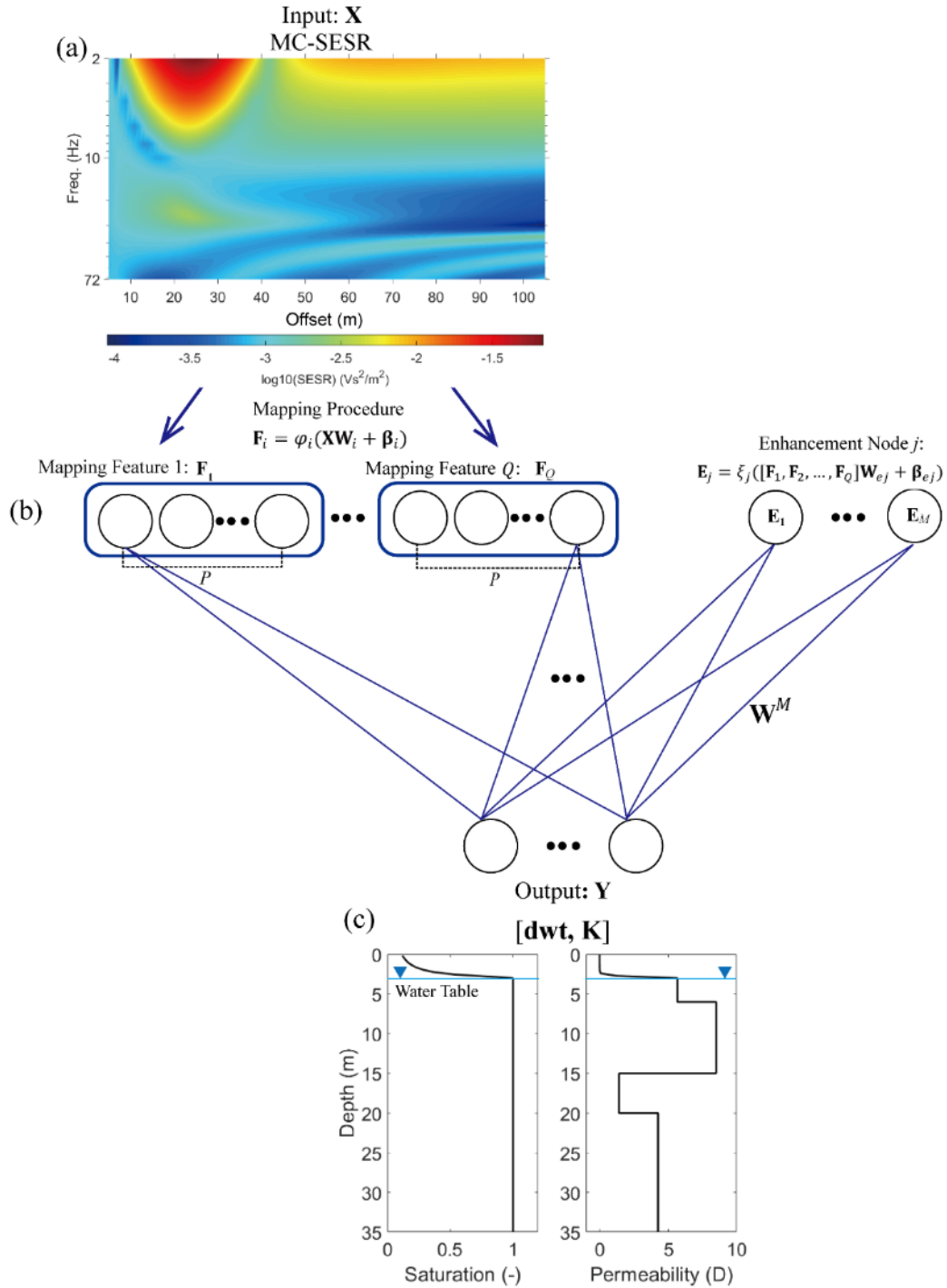
415 Therefore, the training process only needs to estimate the connected-link matrix \mathbf{W}^M through
416 solving the pseudoinverse matrix $[\mathbf{F}^Q | \mathbf{E}^M]^+$:

$$\mathbf{W}^M = [\mathbf{F}^Q | \mathbf{E}^M]^+ \mathbf{Y}. \quad (23)$$

417 Following Chen and Liu (2017), the ridge regression approximation is employed to optimize \mathbf{W}^M
 418 by fulfilling:

$$\arg \min: \|[\mathbf{F}^Q | \mathbf{E}^M] \mathbf{W}^M - \mathbf{Y}\|_2^2 + \lambda \|\mathbf{W}^M\|_2^2, \quad (24)$$

419 where λ denotes a tradeoff regularization factor and $\|[\mathbf{F}^Q | \mathbf{E}^M] \mathbf{W}^M - \mathbf{Y}\|_2^2$ is the error term of the
 420 training set. Except for the connected matrix \mathbf{W}^M , the remaining weight matrices in the network
 421 are randomly generated. Consequently, we can use the well-trained network with the optimal
 422 connected weights \mathbf{W}^M to invert MC-SESRs data. For example, if we acquired more MC-SESRs
 423 data, we just need to replace Input \mathbf{X} with the new (untrained) data in Equation 20. By following
 424 similar computations to the training process by Equations 20-22, we then extract the mapping
 425 features of the inversion data and use an activation function to learn these features in the
 426 enhancement layer. Thus, we obtain the newly mapped feature matrices and enhancement
 427 matrices. Multiplied with the weight matrix derived from the training process (Equations 23 and
 428 24), we can obtain the estimated water table depth and permeability (Equation 22).



429

430 **Figure 2.** Broad learning (BL) procedure including (a) the input (MC-SESr data) layer, (b) the
 431 mapping feature layer and the enhancement layer, and (c) the output (permeability with water
 432 table) layer employed in this study.

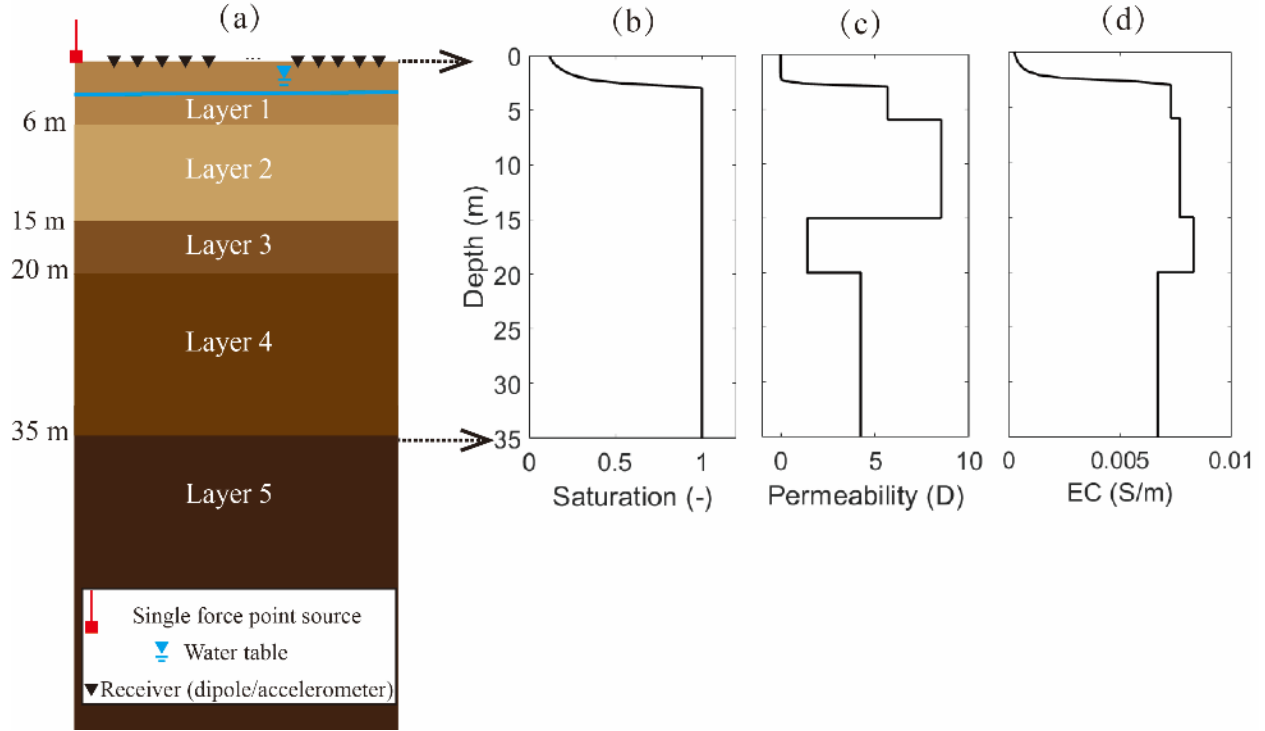
433 **3. Sensitivity Analysis**434 **3.1. Basic test model**

435 We first design a basic test model (Figure 3). It consists of five horizontal layers of
 436 porous materials. It is assumed that the shallow two layers (layers 1-2) are mainly made up of
 437 loamy sands, and the deeper two-layer soils (layers 3-4) with lower permeabilities considered as
 438 silty sands. The bottom layer 5 is assumed as a known layer with lower permeability (0.01 D),
 439 porosity (0.05), and electrical conductivity (16 $\mu\text{S}/\text{cm}$). These hydrogeological parameters are
 440 chosen based on Carsel and Parrish (1988). The initial water table is set at 3 m, implying that the
 441 shallowest layer is partially saturated (Figure 3a). The Richards' equation (Richards, 1931) is
 442 used to solve the hydraulic problem in the vadose zone. The Mualem-van Genuchten (MVG)
 443 empirical model (Mualem, 1976; van Genuchten, 1980) is used to estimate the relationship
 444 between the water saturation and the effective permeability with the pore pressure. Based on the
 445 MVG model by introducing the soil-water characteristic parameters α_{VG} (m^{-1}), n_{VG} and $m_{\text{VG}} =$
 446 $1 - 1/n_{\text{VG}}$, the effective water saturation S_e and the static permeability k_0 at partially saturated
 447 conditions are expressed by:

$$S_e = \frac{1}{[1+(\alpha_{\text{VG}}|H_p|)^{n_{\text{VG}}}]^{m_{\text{VG}}}}, \quad (25)$$

$$k_0 = k_0^{\text{sat}} S_e^{\frac{1}{2}} \left[1 - \left(1 - S_e^{\frac{1}{m_{\text{VG}}}} \right)^{m_{\text{VG}}} \right]^2. \quad (26)$$

448 Here, we assume that the absolute pressure head $|H_p|$ (m) in the vadose zone is equal to the
 449 vertical distance between its elevation and the position of the water table (Zyserman et al., 2017).
 450 The effective electrical conductivity is calculated by Equation 7, whose formulas and the used
 451 parameters are given in Table A3 of Appendix A and Table S1 of the Supporting Information).
 452 The water saturation, the effective permeability, and the effective electrical conductivity of the
 453 top four layers are presented in Figures 3b-d under the assumption that the pore water salinity is
 454 homogeneous at 2×10^{-3} mol/L at 293.15 K, respectively. Note that the effect of the salinity at
 455 this level on the fluid mass density is negligible. In contrast, the mass density of the fluid solute
 456 should be considered in a highly saline environment (e.g., Hu et al., 2023). The specific
 457 parameters of each layered material are given in Table 1, whose descriptions can be found in
 458 Table A2 of Appendix A.



459

460 **Figure 3.** Basic test model and its observations. (a) Geometry, (b) water saturation, (c) effective
 461 permeability, and (d) effective electrical conductivity in the top four layers

462

There is a vertical force point source at the ground marked with a red square in Figure 3a.

463

We assume that the seismic source function $f_s(t)$ (N) presents as a Ricker wavelet with a peak

464

frequency f_p of 20 Hz:

$$f_s(t) = -2.506 \times 10^5 \left[1 - 2(\pi f_p)^2 \left(t - \frac{2}{f_p} \right)^2 \right] \exp[-(\pi f_p)^2 (t - \frac{2}{f_p})^2]. \quad (27)$$

465

The spectrum of this zero-phase wavelet is in a range of ~ 70 Hz. This wavelet and its frequency

466

band are usually considered in seismoelectric simulations (e.g., Jardani et al., 2010). Equation 27

467

is applied to calculate the body force of Equation 5 in forward modeling. Receivers are installed

468

at 0.1 m below the ground surface. The offset ranges from 5 – 105 m with 101 horizontal

469

acceleration sensors and 101 horizontal point dipoles. The offset represents the distance between

470

the source and each accelerometer or central point of each dipole. The interval of two adjacent

471

receivers is 1 m (Figure 3a). Please note that the seismic particle velocity $\mathbf{v}(\omega)$ obtained by

472

geophones could also be used to calculate SESRs by transforming $\mathbf{a}(\omega)$ to $i\omega\mathbf{v}(\omega)$. As

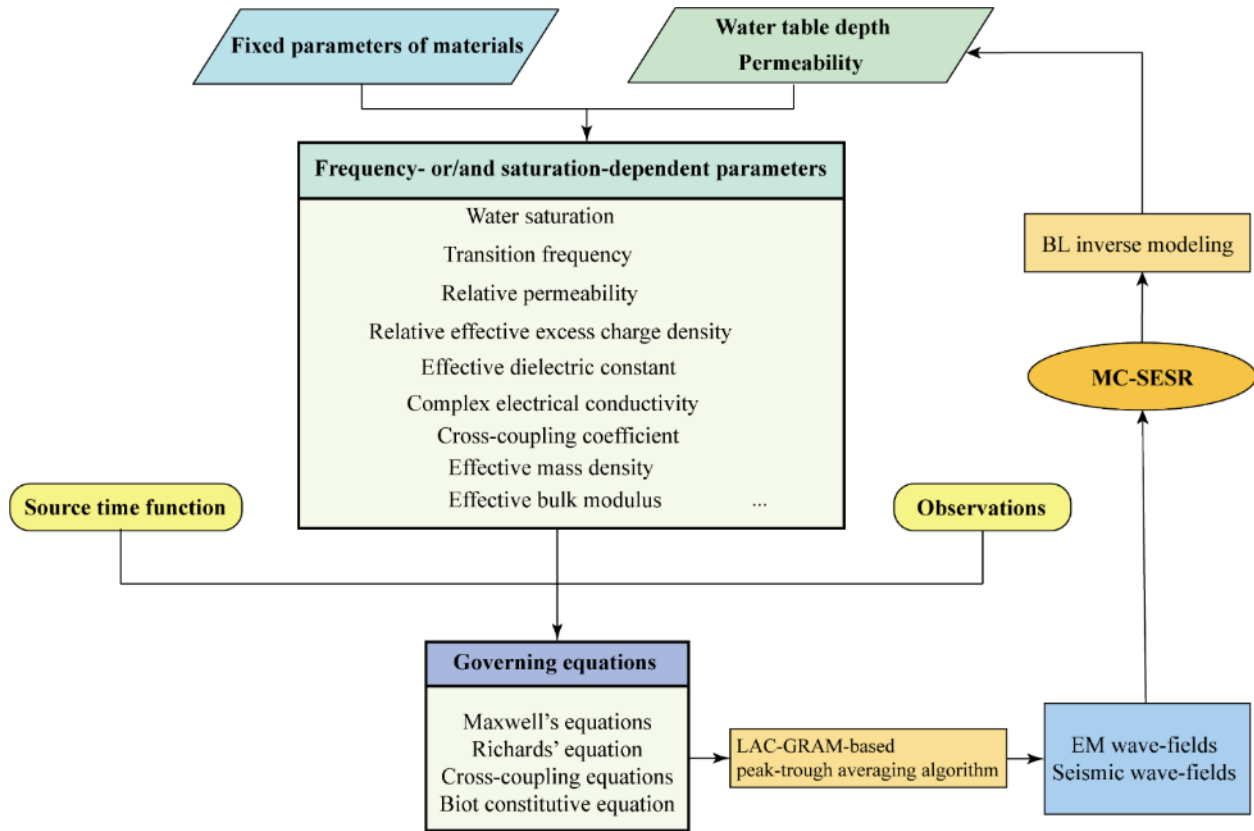
473

mentioned in Section 2.2, measuring SESRs does not require knowledge of the seismic source

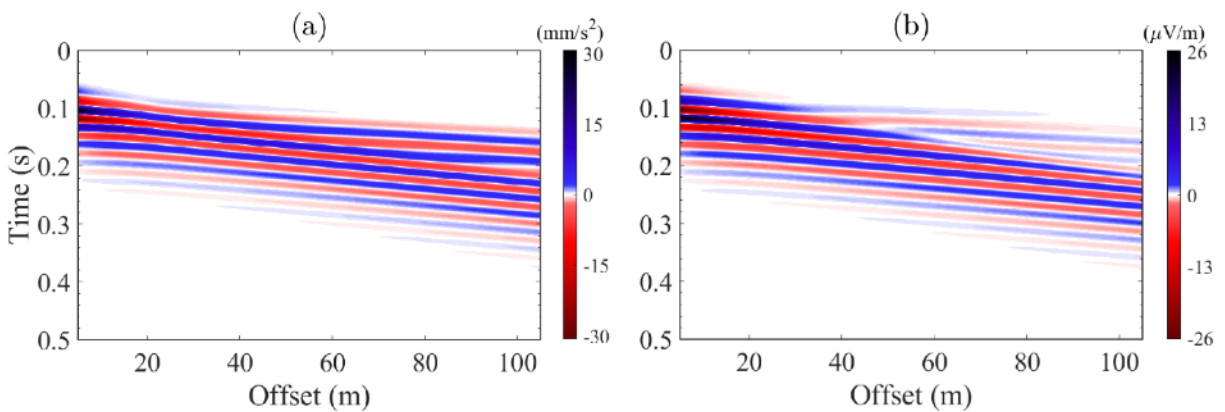
474 function, so we would not need to know the amplitude of the seismic source. Additionally, the
475 SE responses are proportional to the amplitude of seismic sources, either for explosive sources or
476 weight drops, demonstrated in the field tests (Butler et al., 1999). Therefore, according to the
477 specific prospecting conditions, this seismic source function can be replaced with other source
478 functions. However, the seismic strength and waveform used here are adopted to illustrate that
479 the predicted electric fields are expected to be measurable for a reasonable seismic source.

480 Based on Section 2.1, with the dynamic and saturation-dependent parameters chosen,
481 especially the cross-coupling coefficient $L^*(\omega, S_w)$ in Equation 11, the peak-trough averaging
482 approach based on Luco-Apsel-Chen Generalized Reflection and Transmission Method (LAC
483 GRTM) (Zheng et al., 2021) is applied to obtain the frequency solution of the governing
484 equations. The wave-field components are derived from the numerical integral over the
485 wavenumber domain. The integrand includes the Bessel function and exponential terms of fast
486 and slow P , S , and EM waves. Compared with the seismic wavelength, the relatively small
487 source-receiver vertical differences make integrands more intensively oscillate. Therefore, this
488 situation may cause a slow convergence computationally (Zheng et al., 2021). The peak-trough
489 averaging approach uses a certain wavenumber interval in a stably oscillating range to determine
490 peaks and troughs of integrands and subsequently apply the repeat average method to efficiently
491 compute the numerical integration (Dahlquist & Björck, 1974). Thus, it allows us to consider
492 more flexible source-receiver geometries. All used dynamic and saturation-dependent parameters
493 and corresponding formulations are given in Table A3 of Appendix A, and we summarize a flow
494 chart of the model generation in Figure 4. We assume that the data recorded from 0 to 0.5 s is
495 digitized by 4096 samples with a sample interval of 0.1221 ms. After the full-waveform
496 computation of this model, we display the horizontal components of seismic ground acceleration
497 and SE wave fields (Figure 5). Since a zero-phase wavelet was applied to simulate the seismic
498 source (Equation 27), a time delay is shown in the waveforms (Figure 5). In addition, due to a
499 low saturation ($S_w = 0.12$) occurring on the near-surface (~ 0.3 m), the corresponding S -wave
500 velocity is 1242.5 m/s. The surface waves can have a high apparent velocity to present in longer
501 source-receiver offsets than the offset range shown in Figure 5. In this case, the maximum
502 absolute horizontal electric field is 26.27 $\mu\text{V/m}$. Although the electric-field signals are vulnerable
503 to noise, the environmental noise level can be managed to below the order of 0.1 $\mu\text{V/m}$ (see

504 Butler et al., 2007; Dupuis et al., 2007; Thompson & Gist, 1993). The near-surface electric field
 505 of this case is, hence, sufficient to be observed.



506
 507 **Figure 4.** Framework of MC-SESRs generation



508
 509 **Figure 5.** Horizontal components of wave fields under the basic test model (a) seismic ground
 510 acceleration and (b) seismoelectric wave fields

511 The horizontal components of seismic ground acceleration and SE wave fields recorded
 512 in the time domain are subsequently transformed into the frequency domain. Then the MC-
 513 SESRs over the full 0.5s time window are calculated by Equation 19. Here, we take the

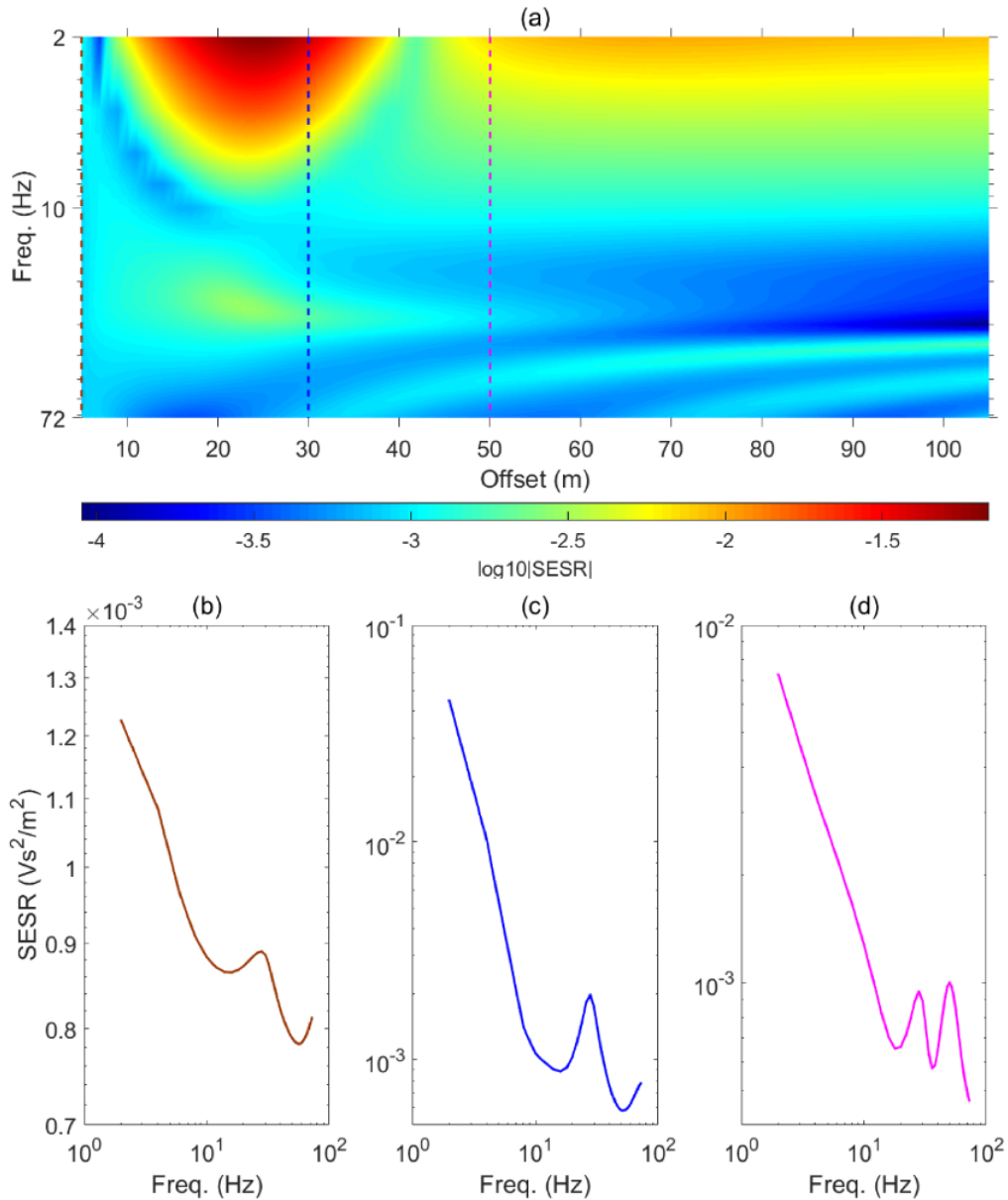
514 frequency in the range of 2-72 Hz. The MC-SESRs' contour map of this numerical model is
 515 shown in Figure 6a. The SESRs with greater strength are mainly distributed in a short-offset
 516 range (10 - 40 m) and a low-frequency range (~ 10 Hz). Since the SESR concept under the
 517 assumption of the localized (coseismic) SE field waves are linear with the ground acceleration,
 518 the frequency-dependent behaviors depend on the evanescent and radiated SE field waves
 519 (Dizeran et al., 2019). The generation of the radiated SE field waves is commonly regarded as
 520 caused by the seismic waves nearly vertically arriving at interfaces and the ground surface.
 521 Although the radiated EM waves generated by the direct SE conversions at the source also
 522 depend on the frequency, their strength is weak. The subsurface properties' variations barely
 523 affect the component of MC-SESRs originating from the direct SE conversions.

524 Once the seismic incident angle is larger than the critical angle θ_c :

$$\theta_c = \arcsin\left(\frac{V_{\text{sei}}}{V_{\text{EM}}}\right), \quad (28)$$

525 where V_{sei} (m/s) and V_{EM} (m/s) denote the seismic wave velocity and EM wave velocity,
 526 respectively, the SE conversion leads to the generation of evanescent SE waves. Actually, θ_c
 527 approaches zero due to $V_{\text{EM}} \gg V_{\text{sei}}$. The existence of physical properties' contrasts causes the
 528 interfacial SE responses, mainly containing evanescent SE field waves. The superposition of
 529 different modes of SE conversions makes the spectral ratios between the SE responses and the
 530 ground acceleration are of frequency dependence. Thus, the SESR modulus decreasing with the
 531 increasing frequency mainly attributes to the evanescent SE waves, which approximately decay
 532 with a factor $\exp(-\omega p \Delta z)$ (Ren et al., 2018). The horizontal EM wave slowness p relies on the
 533 incident angle of the seismic waves arriving at the interface and inducing the localized SE waves.
 534 The spatial variations of SESRs presumably are complicated due to the presence of a vadose
 535 zone. The multi-channel SE field waves combined with the ground acceleration field waves are
 536 sensitive to water table variations (e.g., Rabbel et al., 2020). Using MC-SESRs facilitates the
 537 inversion of hydrogeological parameters due to without reconstructing the seismic source
 538 function. Selecting SESRs from near- and far-offset receivers, we show the SESRs varying over
 539 frequency for three receivers with different offsets of 5 m, 30 m, and 50 m, respectively. As
 540 shown in Figures 6b-d, the SESRs at different offsets have a similar frequency dependence. The
 541 SESR generally increases as the frequency decreases, and their log-scale variations show an

542 approximately linear correlation in the low-frequency domain (~ 10 Hz), and it oscillates at
 543 higher frequencies. Notably, the oscillating signatures are more notable in the far-offset range
 544 (Figures 6c-d). These oscillatory characteristics may originate from the electric field induced by
 545 the guided P -wave traveling in the upper two layers.



546

547 **Figure 6.** The MC-SESRs of the basic test model with (a) the contour map of MC-SESRs in
 548 logarithmic scale showing variations both with frequency and offsets. Sample SESR curves as a
 549 function of frequency at different offsets: (b) 5 m, (c) 30 m and (d) 50 m.

550

551 **Table 1**552 *Parameters of the basic test model*

Property	Units	Layer 1	Layer 2	Layer 3	Layer 4	Layer 5
Thickness	m	6	9	5	15	Inf.
ϕ	m ³ /m ³	0.41	0.43	0.46	0.38	0.05
α_{VG}	m ⁻¹	12.4	-	-	-	-
n_{VG}	-	1.89	-	-	-	-
S_{wr}	-	0.1585	-	-	-	-
ρ_s	kg/m ³	2650	2650	2650	2650	2700
ρ_w	kg/m ³	1000				
ρ_a	kg/m ³	1.21	-	-	-	-
ρ_b^{sat}	kg/m ³	1973.5	1940.5	1891	2023	2615
C_w	mol/L	2×10^{-3}				
σ_0^{sat}	S/m	0.0073	0.0077	0.0083	0.0067	0.0016
η_w	Pa·s	1×10^{-3}				
η_a	Pa·s	1.8×10^{-5}	-	-	-	-
T	K	293.15				

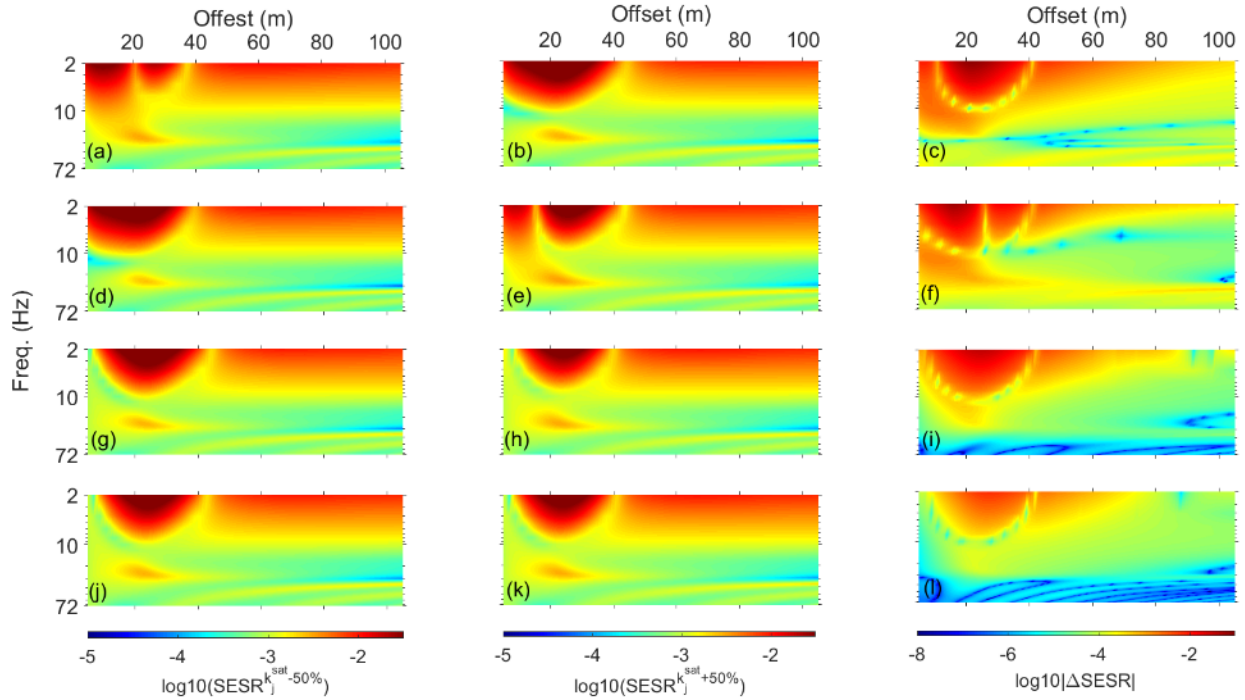
κ_s	-	4				
κ_w	-	80.1				
κ_a	-	1				
m	-	1.35				
n	-	1.85				
K_s	GPa	35	35	35	35	36
G	GPa	2.49	2.49	14.08	14.08	15
K_{fr}	GPa	2.84	2.84	14.4	14.4	20
K_w	GPa	2.25				
K_a	Pa	1.43×10^5	-	-	-	-

554 **3.2. Analysis of permeability**

555 First, we test the sensitivity of SESRs with respect to permeability. The considered
 556 typical ranges in the critical zone refer to Carsel and Parrish (1988). The saturated permeability
 557 k_j^{sat} of the top four layers ($j = 1,2,3,4$) in the basic test model is 5.67, 8.51, 1.42, and 4.26 D,
 558 respectively (Figure 3c). By changing the saturated permeability of shallow layers ($j =$
 559 $1,2,3,4$) $\pm 50\%$, we calculated the absolute MC-SESRs difference concerning the original model
 560 by:

$$\Delta\text{SESR}(\omega, x_i, j) = \left| \text{SESR}(\omega, x_i)^{k_j^{\text{sat}+50\%}} - \text{SESR}(\omega, x_i)^{k_j^{\text{sat}-50\%}} \right|, \quad (29)$$

561 where the horizontal offset x_i ranges from 5 to 105 m with the number of receivers $i =$
 562 $1,2, \dots, 101$. The short-offset (~ 20 m) SESRs have more changes when the permeability of
 563 shallow layers has been changed than the permeability of deep layers has been changed (Figure
 564 7). Their maximum absolute differences with changing the saturated permeability of each layer
 565 decrease in depth, which is 0.0877, 0.0636, 0.0377, and 0.0069 (Figures 7c, 7e, 7h, and 7l),
 566 respectively. The MC-SESRs mainly change in near-offset traces ($x_i < 45$ m) and low frequencies
 567 ($f < 10$ Hz). The absolute differences of SESRs are less when the permeability in the lower zone
 568 changes (Figure 7l), whose maximum absolute difference of SESRs is an order of magnitude
 569 smaller than for layers 1 and 2. As shown in Figure 7, by changing the permeability of different
 570 layers, the absolute differences of SESRs produce different variations either in frequency or
 571 laterally.



572

573 **Figure 7.** The MC-SESRs in logarithmic scale with respect to (a-d-g-j) 50% decrease and (b-e-h-
 574 k) 50% increase the basic test model of (a-c) layer 1, (d-f) layer 2, (g-i) layer 3, and (j-l) layer 4.
 575 (c-f-i-l) The absolute MC-SESRs difference in logarithmic scale of the corresponding layers
 576 calculated by Equation 29.

577

578

579

580

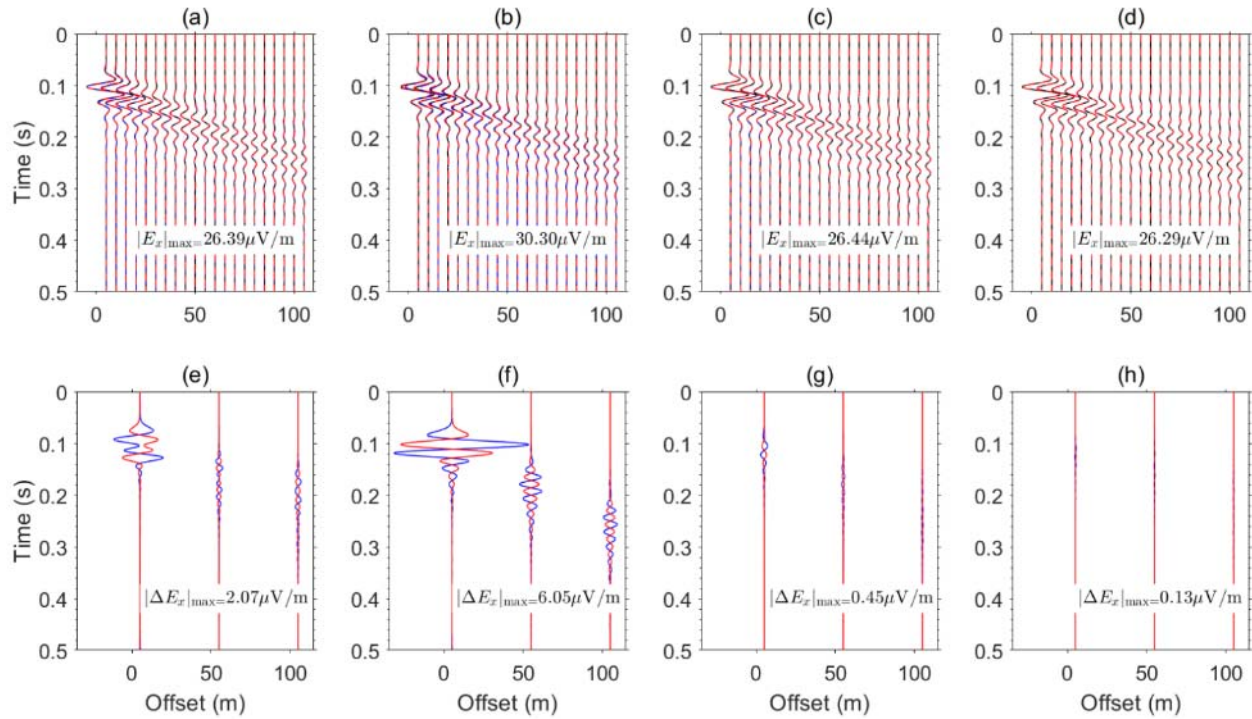
581

582

583

584

To test the behaviors of SE wave-fields by changing the permeability of each layer, we compare the differences between the original waveforms with the changed waveforms in Figure 8. As shown in Figures 8e-h, the variations of SE wave fields are largest when the permeability of layer 2 changes (Figures 8b and 8f). Layer 2 is saturated and provided with the highest saturated permeability in the basic test model. Interestingly, the differences by changing the permeability of layer 1 (Figure 8e) show a very different trend within 0.06 – 0.14 s in contrast with other layers (Figures 8f-h). Layer 1 is a partially saturated zone, which produces a different behavior on waveforms compared with other layers.



585

586 **Figure 8.** (a-d) Horizontal components of SE wave fields for the basic test model (black solid
 587 lines) and for cases of 50% increase (red lines) and decrease (blue lines) in the permeability of
 588 layers 1-4 respectively. (e-h) Differences between SE wave fields obtained for cases of 50%
 589 increased (red lines)/decreased (blue lines) permeability in layers 1-4 respectively compared to
 590 those obtained for the original model, at three particular offsets, whose amplitudes are amplified
 591 by a factor of 8 compared to those in (a-d).

592

3.3. Analysis of water table

593

594

595

596

597

598

599

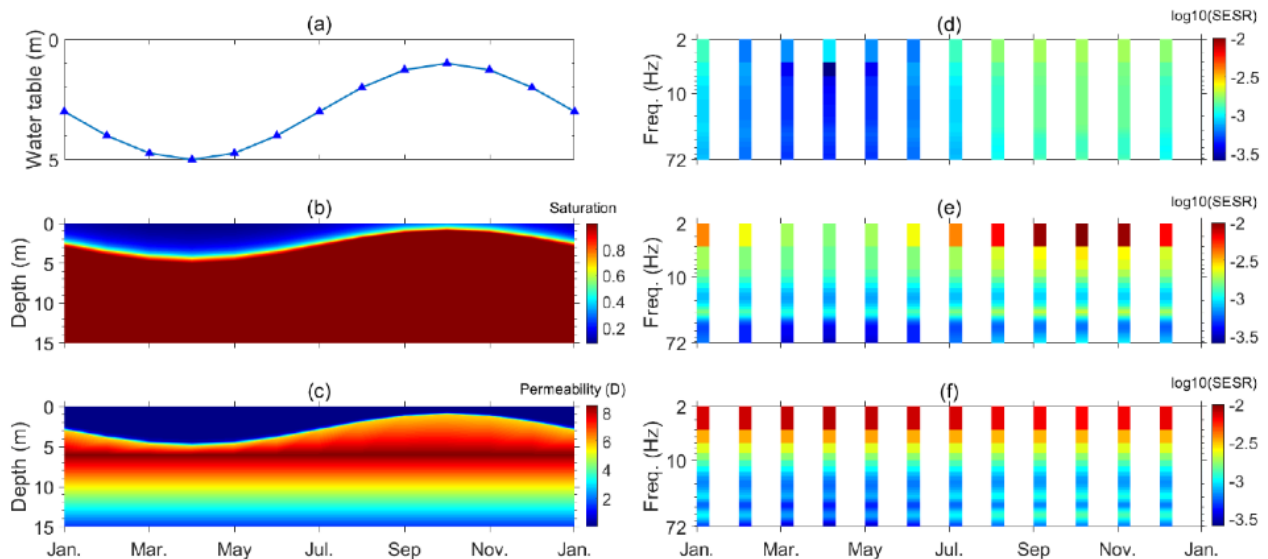
600

601

Second, we test how the different depths of the water table or partially-saturated conditions influence the distributions of MC-SESRs. Accounting for a static partially-saturated state, the VG model is used to determine the water saturation (van Genuchten, 1980). The water table of the basic test model is assumed to vary seasonally in a year. In this case, we assume the rainy season is from September to November with higher water levels, and the period of March to May is the dry season with lower water levels (Figure 9a). Correspondingly, the water saturation and the effective permeability at the shallow layer change with the water table (Figures 9b-c). As the used parameter α_{VG} (12.4 m^{-1}) of the VG model is large, the permeability is rather low at low saturations. Note that the contour map of permeabilities shown

602 in Figure 9c is an interpolation result in the time and space domain. Permeabilities below the
 603 water level in each layer are different constants, as the basic test model presented in Figure 2c.
 604 The SESRs with the short (5 m), medium (30 m), and long (50 m) source-receiver offset are
 605 collected to show their responses to the variations of the water table (Figures 9d-f). The absolute
 606 ratios increase in the rainy season with higher water levels and decrease in the dry season with
 607 lower water levels.

608 Furthermore, the strength of SESRs in the high-frequency domain is increased when the
 609 water table is in the shallow zone (e.g., September-November). The amplitudes of evanescent SE
 610 signals decay exponentially with the normal direction of the interfaces (Ren et al., 2016b; Ren et
 611 al., 2018). This implies that deep water tables cause weaker SE signals than shallow water tables.
 612 This characteristic is also embodied in the SESRs data obtained at the source-receiver offset of
 613 30 m (Figure 9e). Nevertheless, the sensitivity of the SESRs obtained at a more extended offset
 614 (50 m) responding to the dynamic water table depth is considerably weakened (Figure 9f). This
 615 test implies we may use the time-lapse MC-SESRs data in short source-receiver traces to monitor
 616 the water table depth variations.



617 **Figure 9.** The modeling results with the water table vary over time. (a) The depth of the water
 618 table, (b) the time-lapse variations of the water saturation with depth, (c) the effective
 619 permeability, and the SESRs in logarithmic scale collected at a source-receiver distance of (d) 5
 620 m, (e) 30 m and (f) 50 m.
 621

622 4. Inversion Results

623 Employing synthetic seismic and SE data generated for the basic test model introduced in
 624 Section 3.1, we carry out a three-step strategy to perform MC-SESRs inversion. We assume that
 625 the depth and properties of the bottom layer 5, and all other layer depths and properties except
 626 for the water table depth and the permeabilities of layers 1-4 are known. The prior information
 627 could have been determined by drilling and other geophysical methods (e.g., Dzieran et al,
 628 2019). This could represent a scenario where there was interest to monitor temporal changes in
 629 depth to the water table and to determine permeabilities of the near surface layers (to 35 m
 630 depth) for hydrogeological applications.

631 To begin, we generated random samples by drawing permeabilities for each of layers 1 -
 632 4 from predefined reasonable ranges, and drawing a water table depth in layer 1 randomly from
 633 the range of 1 - 5 m. We account for the ranges of hydraulic conductivity K_j^{sat} of layers 1-2,
 634 referring to materials consisting of loamy sands. Layers 3-4 with a lower range of the soil
 635 permeabilities are considered to contain more silty sands (Carsel & Parrish, 1988). The hydraulic
 636 conductivity of layers 1-2 ranges from 3 to 35 cm/h and layers 3-4 ranges from 0.02 to 15 cm/h,
 637 which can be transformed to the ranges of permeability k_j^{sat} by is equal to $\frac{K_j^{\text{sat}}\eta_w}{\rho_w g}$, where g
 638 (m/s^2) denotes the gravitational acceleration (9.81 m/s^2). Following the flowchart of the model
 639 generation (Figure 4), we calculated MC-SESRs of 7000 random samples. Therefore, the first
 640 step is to obtain the 7000 input-output pairs.

641 4.1. Performance of the BL neural network

642 In the second step, we randomly selected 5000 from the 7000 input-output pairs for
 643 training the BL neural network (Figure 2). In addition, 1500 randomly generated samples were
 644 split into the original validation dataset (500 samples) and the original testing dataset (1000
 645 samples). The input MC-SESRs data of the training samples are noise-free synthetic data, and
 646 output data are the dwt and the permeability of layers 1-4 (k_1, k_2, k_3, k_4) (Figure 2c). First, to
 647 accurately extract and map features of the input data, we need to set the number of mapping
 648 groups (Q) and feature nodes (P) of each group and their corresponding enhancement nodes (M)
 649 based on the BL architecture (Figure 2) introduced in Section 2.3. After that, the BL network is

650 fixed. We tested different configurations of the BL neural network to present the root-mean-
 651 squared errors (RMSEs) of training models (water table depth and permeability):

$$RMSE^j = \sqrt{\frac{\sum_1^n (\text{Output_}Y_i^j - \text{True_}Y_i^j)^2}{n}}, \quad (30)$$

652 where j denotes the corresponding numbers of different parameters ($j = 1$ for dwt, and $j = 2 - 5$
 653 for k1-4 respectively). n is the number of samples for training the network, which is 5000 in this
 654 case. $\text{Output_}Y_i^j$ and $\text{True_}Y_i^j$ are the reconstructed and true output of the j th parameter of the
 655 i th sample. Here, we separately present the RMSEs of different parameters since the output
 656 dataset indicate different properties and in different scales. The ranges of P , Q and M are
 657 [10:5:100], [10:5:100], and [10:10:500], respectively. The regularization coefficient is set to
 658 10^{-8} (see Chen & Liu, 2017). The optimum sets of parameters for training models are given in
 659 Table 2. The RMSEs of water table depth can be limited to 0.034 m. The RMSEs of permeability
 660 of layer 1 are much higher than layers 2-4. In contrast with deep layers, the permeability of the
 661 top layer is easier to be directly investigated in situ. k2 and k3 reach their optimum under $P=15$,
 662 $Q=10$ and $M=500$, and correspondingly, the RMSEs for estimating the dwt and k4 are
 663 satisfactory with the same setting.

664 **Table 2**

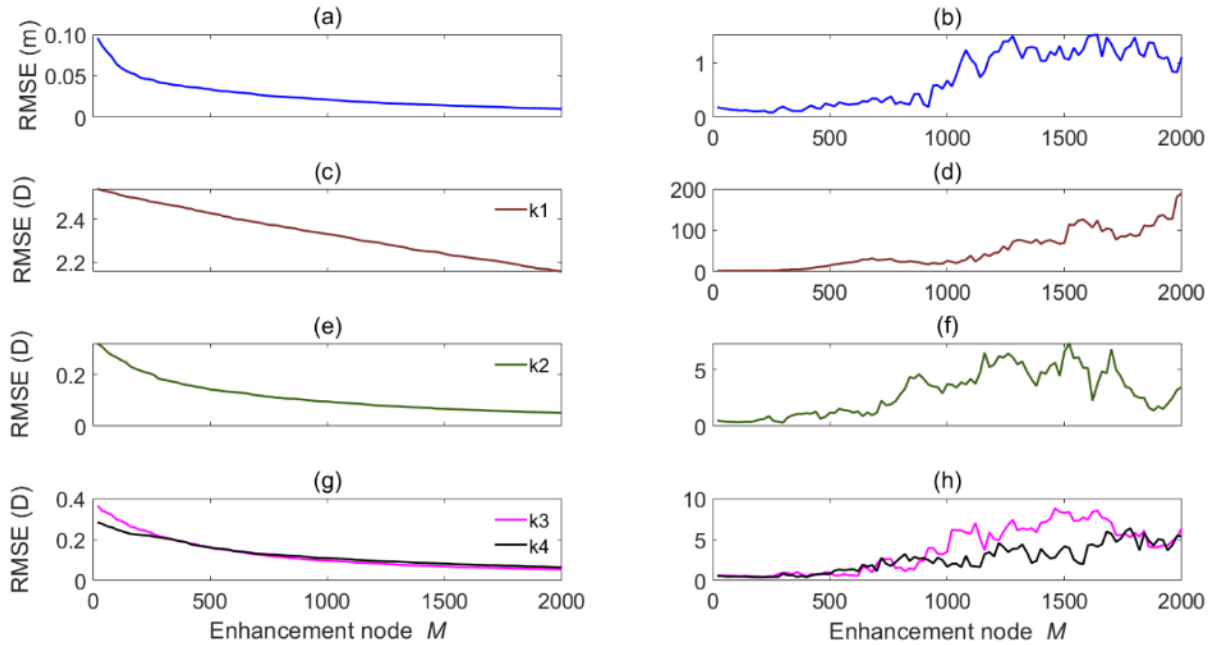
665 *RMSEs of training data set with different configurations of the BL model (bold numbers denote*
 666 *the corresponding minimum RMSEs)*

Parameters of BL model			RMSE of training models				
P	Q	M	dwt (m)	k1 (D)	k2 (D)	k3 (D)	k4 (D)
100	100	500	0.0210	2.4174	0.1462	0.1899	0.1526
80	40	500	0.0271	2.4090	0.1713	0.2005	0.1644
15	10	500	0.0339	2.4274	0.1415	0.1603	0.1616
10	10	500	0.0336	2.4239	0.1473	0.1628	0.1500

667 As the parameters' estimation accuracy is the highest when the number of enhancement
 668 nodes (M) reaches the maximum in the search range, we expanded this range to search for an
 669 appropriate neural network. The neural network gets more complex structures with a large
 670 number of groups, mapping feature nodes, and enhancement nodes, which may empower the BL
 671 model to describe the approximate mapping relationship between the input and output data from

672 the training data set. As shown in Figure 2b, M directly reflects the complexity of the connected
673 matrix for linking the integration of the feature mapping layer and the enhancement layer with
674 the output layer. To examine whether the RMSEs would be reduced by keeping increasing the
675 enhancement nodes and fixing $P = 15$ and $Q = 10$, we display the RMSEs varying with the
676 number of enhancement nodes (Figure 10). In addition, we utilized 500 untrained samples from
677 the validation dataset to test the inverted performance with increasing M . Further, the measured
678 data in practice ineluctably contain some noise. With the improvement of pre-and post-
679 processing techniques on near-surface SE applications, the signal-to-noise ratio (SNR) can be
680 achieved to 20 – 45 dB (Butler & Russel, 2003; Butler et al., 2007). Thereby, to account for the
681 possible interferences from self-noise and background noise, we add 5% random noise of the
682 mean amplitude of synthetic SESRs at each trace (SNR \approx 26 dB) to the initial validation and
683 testing datasets without noise contamination. Similar to the treatment of the training dataset, the
684 RMSEs of the validation dataset are calculated by replacing the number of samples in Equation
685 30 to 500 and updating the corresponding output dataset. Slightly though, the RMSE set keeps
686 decreasing with M increasing (Figures 10a, 10c, 10e, and 10g), which indicates the neural
687 network has been adapted to the training data set. However, there are different trends shown in
688 untrained samples (Figures 10b, 10d, 10f, and 10h).

689 The parameter estimation using untrained noisy data as input performs better when M is
690 lower than 300 (Figures 10b, 10d, 10f, and 10h). The number of enhancement nodes of each
691 parameter reaching a minimum RMSE is given in Table 3. To show the influence of chosen M
692 on the inversion accuracy, we contrast the true and reconstructed models by inputting noisy MC-
693 SESRs of the validation dataset under the BL neural networks trained by $M = 50, 200, 500,$ and
694 1000, respectively. Taking the water table depth as an example to display (Figure 11), the
695 majority of reconstructed models are visually closer to the true models with increasing M , but the
696 RMSE increases when $M \geq 200$ (Figures 11c-d). The reconstructed permeability also presents a
697 similar trend (see Figures S1-S3 of Supporting Information). It can be attributed to the large
698 departure of a few estimations from the true models. Finally, to detect the dynamic water table,
699 we choose $M = 240$ as the number of enhancement nodes to train the BL model.



700

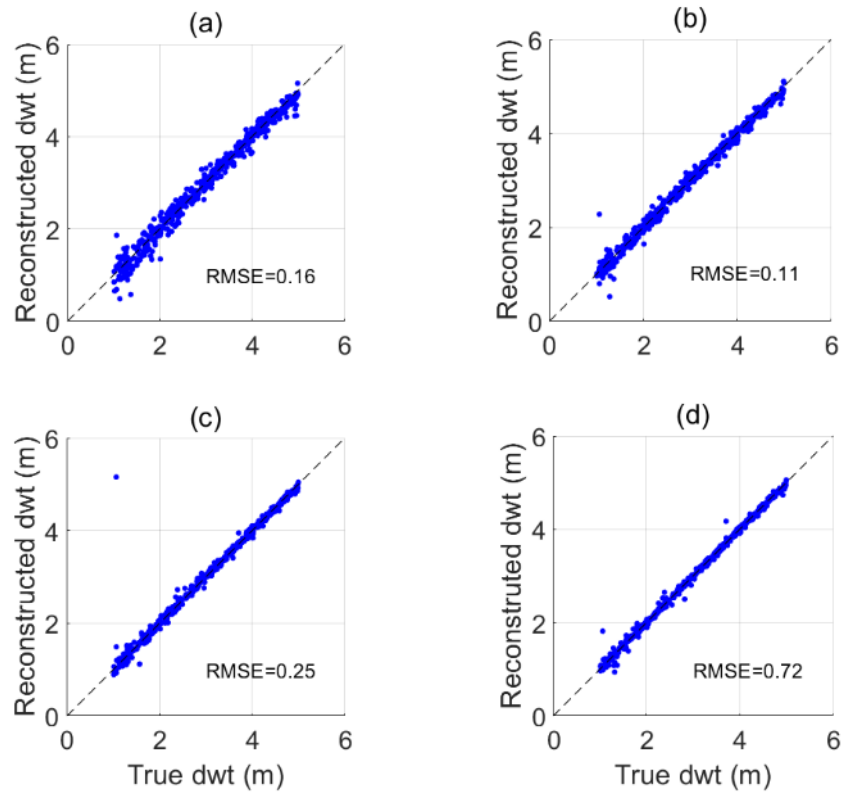
701 **Figure 10.** RMSEs of output data (a-b: water table depth, c-d: permeability of layer 1, e-f:
 702 permeability of layer 2, and g-h: permeability of layers 3-4) vary with the number of
 703 enhancement nodes ($P=15$, $Q=10$). Panels in the left column (a, c, e, g) represent the training
 704 data set and panels in the right column (b, d, f, h) represent the validation noisy dataset.

705 **Table 3**

706 *RMSEs of validation data set with the optimum number of enhancement nodes (bold numbers*
 707 *denote the corresponding minimum RMSEs)*

Enhancement node	RMSE of validation models				
	dwt (m)	k1 (D)	k2 (D)	k3 (D)	k4 (D)
M					
240	0.0895	2.7884	0.8879	0.5321	0.4339
20	0.1839	2.6092	0.4798	0.6212	0.5654
300	0.1945	4.5221	0.3084	0.9505	0.8540
220	0.1196	2.7551	0.6383	0.4510	0.4140
200	0.1117	2.8753	0.5839	0.4730	0.4101

708



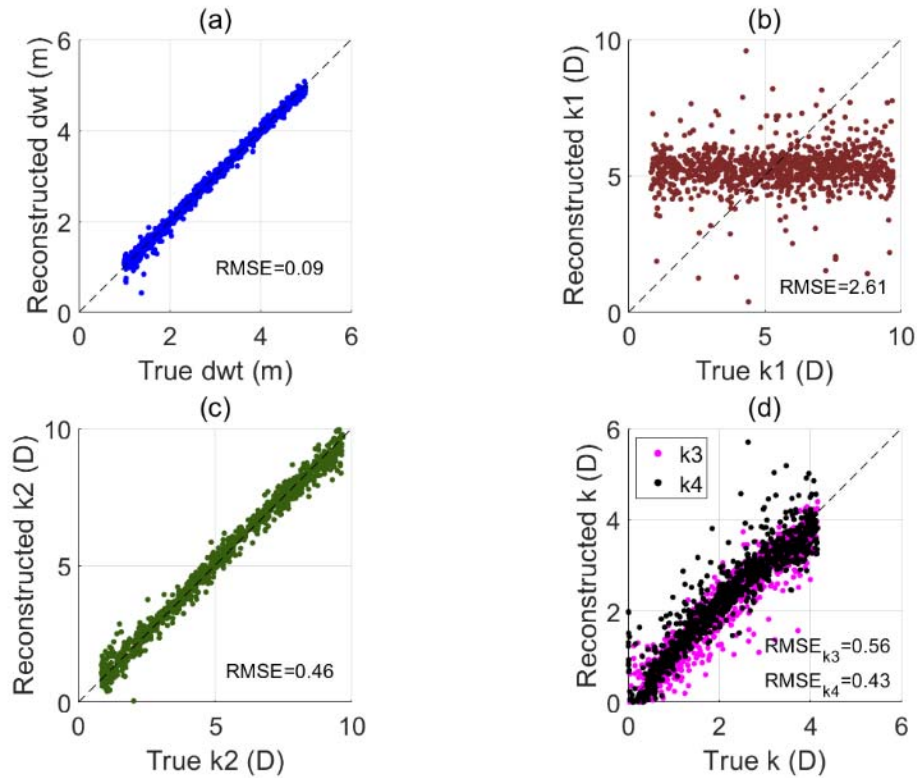
709

710 **Figure 11.** Comparisons of the true and reconstructed depth of water table (dwt) of the validation
 711 dataset with (a) $M = 50$, (b) $M = 200$, (c) $M = 500$, and (d) $M = 1000$

712 4.2. Comparisons of reconstructed and true models

713 After the 500 validation samples validated the BL model obtained by the 5000 training
 714 samples, we took the third step to attain MC-SESRs inversion. We applied this BL neural
 715 network configured by $P=15$, $Q=10$, and $M=240$ to invert the water table depth and permeability
 716 of 1000 testing samples with the same amount of noise contamination as the original testing MC-
 717 SESRs dataset. The testing dataset is independent of the training or validation datasets. The
 718 RMSEs of the testing dataset are calculated similarly to the validation dataset (Equation 30). The
 719 reconstructed depth of the water table has great consistency with corresponding true values
 720 (Figure 12a), whose RMSE is 0.09 m. The inversion results can nicely reconstruct the
 721 permeability of layer 2 (Figure 12c), whose RMSE is 0.46 D. the reconstructed permeability of
 722 layers 3 and 4 deviates more from true values than layer 2 (Figure 12d), while their RMSEs are
 723 acceptable (0.56 D and 0.43 D, respectively). Nevertheless, the permeability of the partially

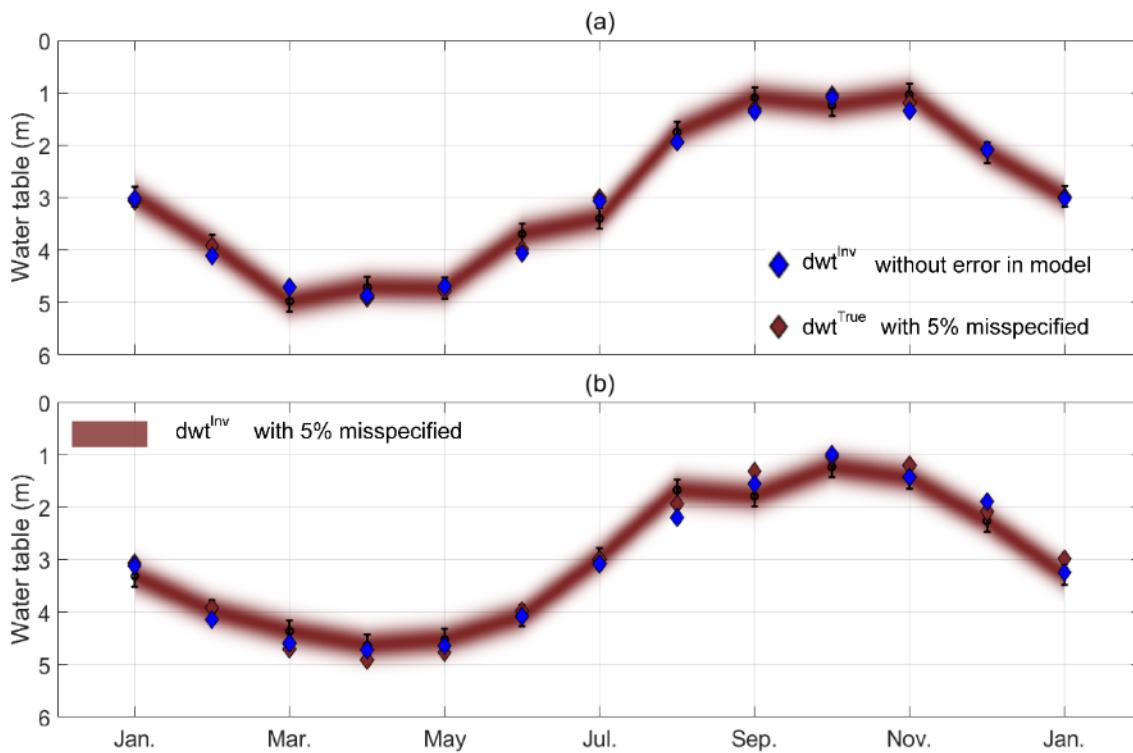
724 saturated layer 1 cannot be reconstructed, which concentrates around 5 D. It reflects that the
 725 SESRs data did not constrain the permeability of the unsaturated layer well since the low
 726 saturation makes a very low effective permeability to obtain a small SE coupling coefficient
 727 (Equation 11).



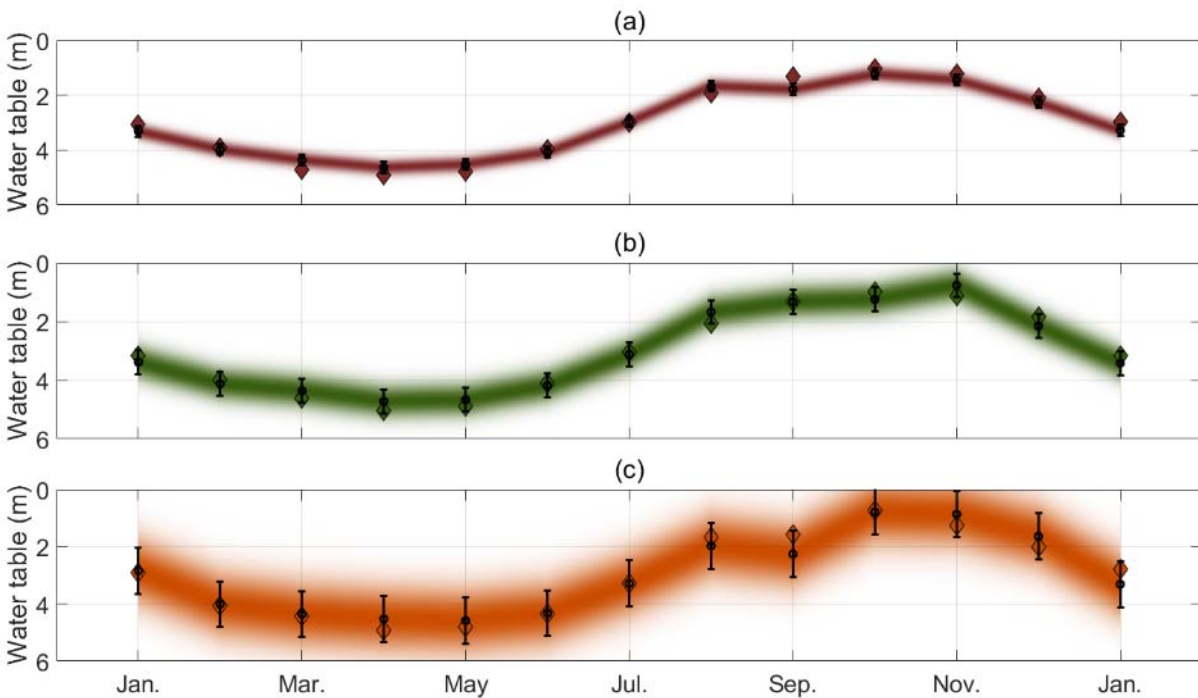
728
 729 **Figure 12.** Comparisons of the true and reconstructed (a) depth of water table, (b) permeability
 730 of layer 1, (c) permeability of layer 2 and (d) permeability of layers 3-4 using noisy MC-SESRs
 731 data (SNR \approx 26 dB).

732 Based on the settings of the basic test model, we used the SESRs data introduced in
 733 Section 3.3 to characterize variations in the water table depth. As the data uncertainty not only
 734 can originate from the noise but also possibly contains the errors of the model parameters, here,
 735 we assumed five-percent errors of dwt, permeability, and porosity included in the basic test
 736 model. Still, the data are assumed to be contaminated by five-percent random noise in the
 737 following tests. Meanwhile, as the sensitivity analysis of SESRs to the dwt in Section 3.3 shows,
 738 the short-offset SESRs are more sensitive than the long-offset SESRs to the variations of dwt, we
 739 test to apply the different number of channels to reconstruct the dynamic dwt. All 101 channels'
 740 or 26 short-offset channels' SESRs data used to invert the dwt can obtain comparable accuracy

741 under five-percent errors in model parameters (Figure 13). This test indicates that we can
 742 reconstruct dynamic shallow dwt by using less short-offset MC-SESRs data. Since higher errors
 743 may occur in realistic measurements, we compare the inversion accuracy under five-percent, ten-
 744 percent, and twenty-percent errors in the pre-defined model using 26 short-offset channels'
 745 SESRs in Figure 14. The inverted water table depths are more deviated from the true values by
 746 enhancing errors. However, the overall inverted values are consistent with the true values with
 747 twenty-percent errors in the known model parameters, except for the result in September (Figure
 748 14c).



749
 750 **Figure 13.** Detection of the water table depth using noisy MC-SESRs data collected from (a) 101
 751 traces (5 - 105 m) and (b) 26 traces (5 - 30 m). The blue diamonds represent the inverted value
 752 without the model errors; The red diamonds represent the true values with 5%-misspecified
 753 errors in pre-defined model parameters; The circles represent the inverted values, whose
 754 misspecified levels are indicated by the shaded areas and error bars.



755

756 **Figure 14.** Detection of the water table depth using the noisy 26-channel SESRs data with
 757 misspecified errors of (a) 5%, (b) 10%, and (c) 20% in pre-defined model parameters. Diamonds
 758 represent the true values; The circles represent the inverted values, whose misspecified levels are
 759 indicated by the shaded areas and error bars.

760

761

762

763

764

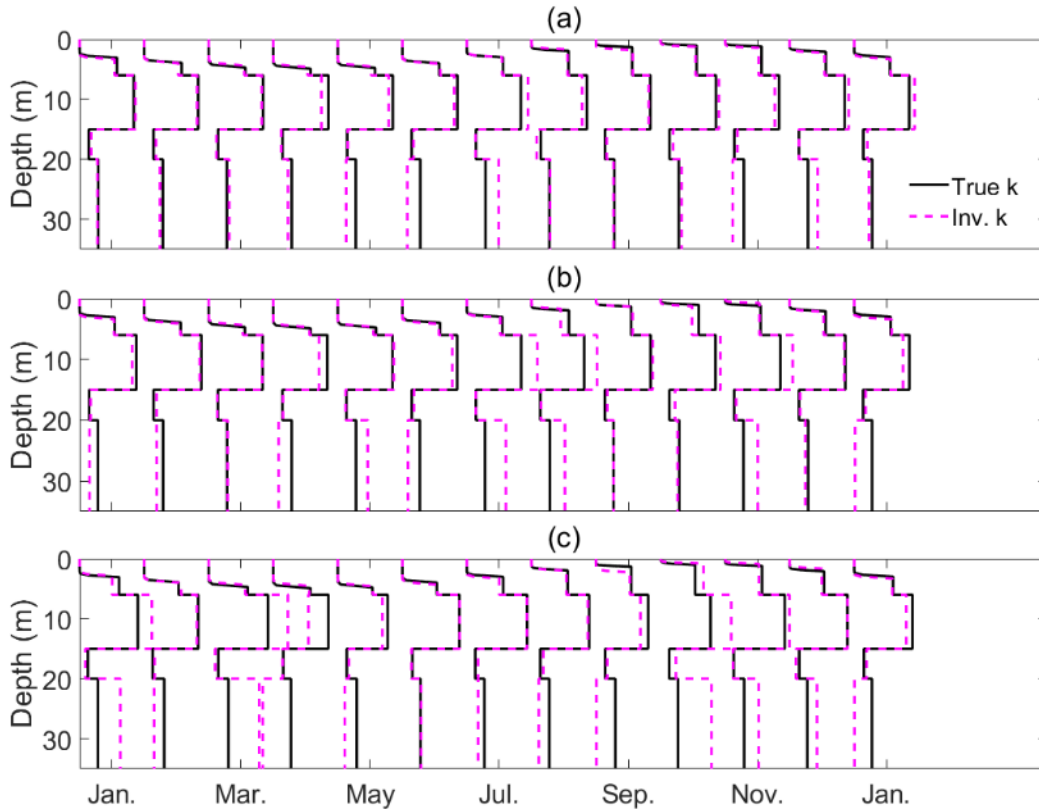
765

766

767

768

As the absolute pressure head in the vadose zone is assumed to be the distance between its elevation and the water table level, the effective permeability and water saturation are calculated by the MVG model. We show that the true and the inverted permeabilities vary with time in Figure 15. The permeability can still be reconstructed in the time-lapse profiles (Figure 15a). The predicted accuracy is also reduced when errors added to the model are enhanced (Figures 15b and 15c). Particularly, the inverted errors of permeability increase in layer 4 due to the increasingly attenuated seismic and SE signals strength. The model parameters may be misspecified by larger errors, which causes lower inverted accuracy in deep layers due to the fragile signals.



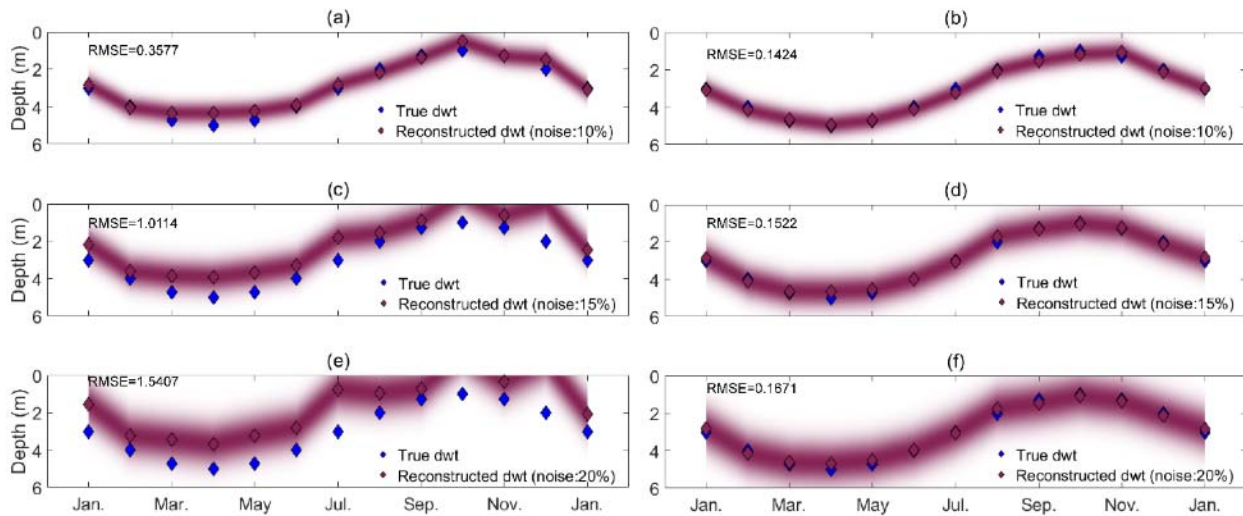
769

770 **Figure 15.** Comparison of true (black lines) and inverted (pink) permeability with the changing
 771 water table depth by accounting for errors of (a) 5%, (b) 10% and (c) 20% in pre-defined model
 772 parameters.

773 5. Discussion

774 To test the capability of this neural network in the presence of noise, we decrease the
 775 SNR to 20 dB, 16 dB, and 14 dB by considering different random noise levels (10%, 15%, and
 776 20%) into synthetic MC-SESRs data. Based on the assumptions in Section 4.3, we attempt to use
 777 the SESRs data at different noise levels to detect the changing water table levels. As shown in
 778 Figure 16, the inverted accuracy is reduced when the noise is enhanced from 5% to 10% and
 779 more. In this case, the water table detection can be achieved at a 10% noise level when 26-
 780 channel SESR data (5 – 30 m) have been involved in the inversion (Figure 16a). This scenario
 781 can be improved by increasing the data by using more traces. The RMSE reaches 0.1671 m at a
 782 20%-noise level when the used channels increase to 101. Correspondingly, the source-receiver
 783 offset ranges from 5 to 105 m (Figures 16b, 16d, and 16f). The inverse modeling may be able to
 784 perform well for stronger noise levels when the used MC-SESR data are sufficient. Note that the

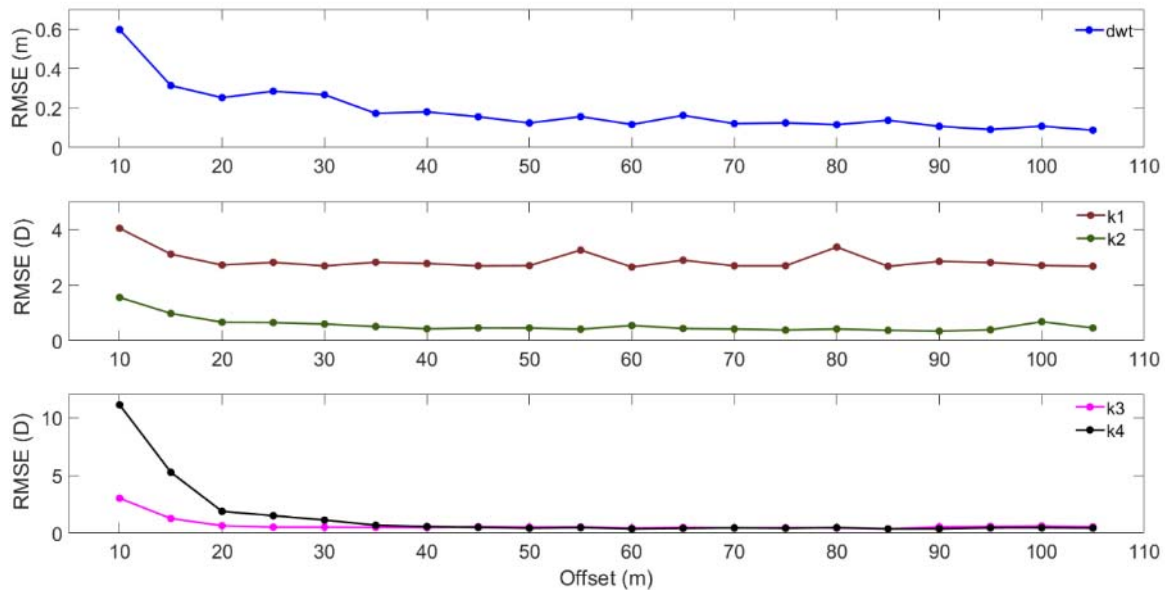
785 monitoring test in Section 4.2 discussed the influence of different levels of errors in model
 786 parameters (Figures 13-15). Ideally, although the water table and permeability changed with time
 787 and contained model perturbations, the well-trained network (Figure 2) can recover their true
 788 values for a specific site. Therefore, the inverted values are still close to the true values using 26-
 789 channel data with mixing the noise level of 5% (Figure 13). However, the porosity of each layer
 790 is also assumed to be misspecified. Thus, the increased errors in the pre-defined model decrease
 791 the inverted accuracy of the water table depth and permeability.



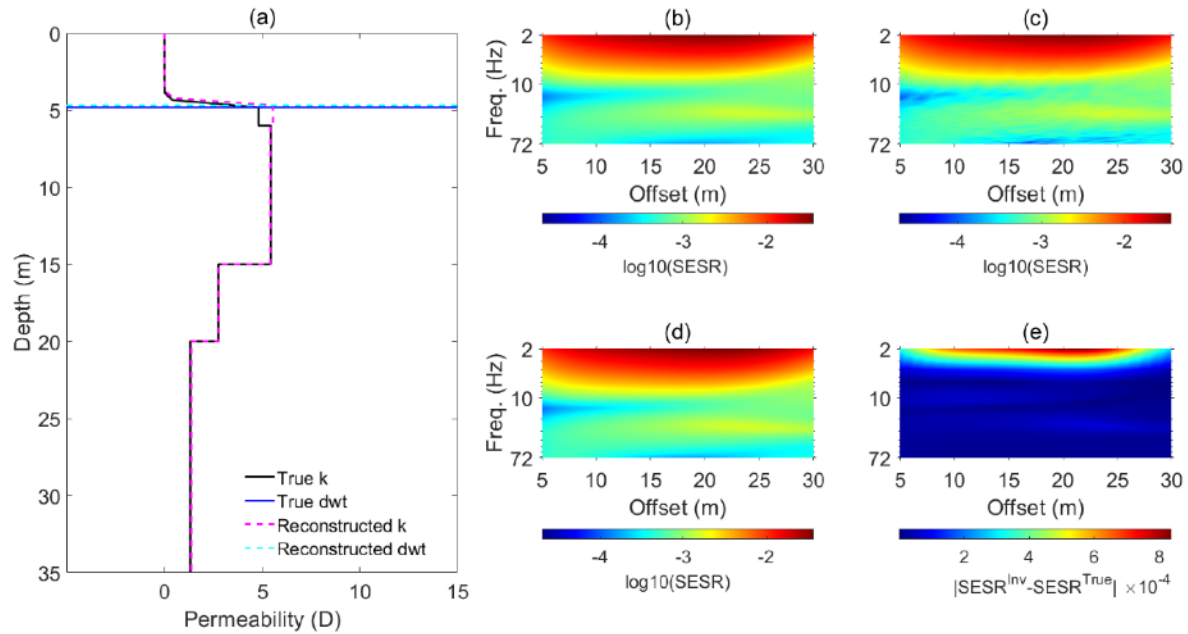
792
 793 **Figure 16.** Comparison of true (blue) and predicted (purple) water table depth by adding (a-b)
 794 10%, (c-d) 15% and (e-f) 20% random noise into data. The left panels (a, c, and e) use 26-
 795 channel SESRs data and the right panels (b, d, and f) use 101-channel SESRs data. The shaded
 796 areas indicate the misspecified levels.

797 As aforementioned sensitivity of permeability and water table depth in Sections 3.2-3.3,
 798 the SESRs at different source-receiver offsets respond to the variations of different layers. The
 799 number and locations of sensors used for inversion may affect the inverted results. We test the
 800 inverted RMSEs using MC-SESRs with different offsets by 1000 untrained random models. The
 801 interval distance of adjacent sensors is kept at 1 m. It starts from offset = 10 m, which means that
 802 MC-SESRs data obtained by 6 traces in the range of 5 – 10 m are used for inversion (see Section
 803 2.3 X: **SESR**_{5000×36×6}). Figure 17 shows that the RMSEs dropped considerably when the used
 804 offsets increased to 30 m, but they continued reducing to a lesser extent. Generally, more SESRs
 805 data used for inversion should obtain higher inverted accuracy.

806 Picking a model to contrast the true with reconstructed parameters, the predicted
 807 permeability can reconstruct the effective permeability above the capillary fringe based on the
 808 water table estimation. However, the predicted saturated permeability of layer 1 deviates from its
 809 true value (Figure 18a). The inverted saturated permeability of the top layer poorly fits the true
 810 value embodied in the whole test set (Figure 12b). As the effective permeability drops
 811 considerably at low water saturations, the SE coupling coefficient is rather small. Thus, the
 812 information of the saturated permeability in layer 1 cannot be extracted by the mapping feature
 813 layer of input MC-SESRs data. The water table depth and permeability of layers 2-4 of the
 814 model are well estimated. Although the noisy MC-SESRs data for inversion are affected by
 815 disturbances (Figure 18c), the MC-SESRs data calculated by the predicted model (Figure 18d)
 816 well fit the synthetic MC-SESRs data (Figure 18b). The fitting errors concentrate in 10 – 25 m
 817 and low frequencies (~ 3 Hz) (Figure 18e). The inversion accuracy for this case is satisfactory by
 818 using data from 26 channels (~ 30 m) to train and invert the water table depth and permeability.
 819 One estimation with lower accuracy is presented in the Figure S4 of Supporting Information,
 820 whose modeling result from the inverted parameters can recover the overall shape and trend of
 821 the original data, but the maximum absolute difference is one order of magnitude larger than
 822 Figure 18e.



823
 824 **Figure 17.** RMSEs between inverted and true models vary with the offset (SNR ≈ 26 dB). (a)
 825 water table depth, (b) permeability of layers 1-2 and (c) permeability of layers 3-4



826

827 **Figure 18.** Comparisons of the true model and the reconstructed model using 26-channel SESR
 828 data. (a) The blue (solid) and cyan (dashed) lines represent the true and predicted water table
 829 depth, respectively. The black (solid) and pink (dashed) lines represent the true and reconstructed
 830 permeability, respectively. (b-d) display the 26-channel synthetic and noisy SESR data modeling
 831 by (b-c) the true model and (d) the inverted model. (e) shows SESRs difference between the data
 832 modeling by the true model and the inverted model.

833 6. Conclusions

834 In this paper, we propose using MC-SESRs to process multi-channel SE signals and
 835 seismic signals recorded at the ground surface. By analyzing the sensitivity of MC-SESRs to the
 836 water table depth and permeability, the results indicate that MC-SESRs data obtained by
 837 different offsets respond to the variations of different water table depths and permeability.
 838 Moreover, we introduce a simple and efficient BL approach to interpret MC-SESRs data to
 839 quantitatively infer the water table depth and permeability of layered-porous materials. As a type
 840 of non-invasive measurement, MC-SESRs obtained by surface observations can supplement
 841 traditional piezometer installations. It can be applied to rapidly and accurately detect the water
 842 table for a specific investigated field even though pre-defined model parameters are misspecified
 843 by 20%. This feature of monitoring the water table has potential applications for assessing
 844 groundwater storage and studying frost thawing and volcanic eruption. Nevertheless, as

845 aforementioned, the dynamic effective excess charge density using the scaling factors by
 846 volumetric average and relaxation time suffers several limits as predictions, particularly at the
 847 pore scale. We suggest considering explicit frequency- and saturation-dependence in the future
 848 (Jougnot & Solazzi, 2021; Solazzi et al., 2022; Thanh et al., 2022).

849

850 **Appendix A**

851 Tables A1 and A2 list the acronyms as well as the notation and description of symbols
 852 used in the manuscript, respectively. The formulations of frequency-dependent (dynamic) and
 853 saturation-dependent parameters are summarized in Table A3.

854 **Table A1.** Acronyms and meaning

Acronyms	Meaning
SE	SeismoElectric
SESR	SeismoElectric Spectral Ratio
MC-SESR	Multi-Channel SeismoElectric Spectral Ratio
EDL	Electrical Double Layer
AVO	Amplitude variation Versus Offset
BL	Broad Learning
RVFLNN	Random Vector Functional Link Neural Network
EM	ElectroMagnetic
MVG	Mualem-van Genuchten
VG	van Genuchten
LAC GRM	Luco-Apsel-Chen Generalized Reflection and Transmission Method
dwt	Water table depth

855 **Table A2.** Nomenclature of the Material Properties

Symbol	Unit	Description
ω	rad/s	Angular frequency
f	Hz	Frequency
ω_t	Hz	Angular transition frequency
θ_c	rad/s	The critical angle of evanescent electromagnetic waves
S_w	-	Water saturation
S_{wr}	-	Residual water saturation
S_e	-	Effective water saturation
σ^*	S/m	Complex electrical conductivity
σ_w	S/m	Electrical conductivity of pore water
σ_0	S/m	Static bulk electrical conductivity
\mathbf{E}	V/m	Electric field
\mathbf{J}	A/m ²	Total current density
L^*	A/m ²	Streaming cross-coupling coefficient
L_0^{sat}	A/m ²	Streaming cross-coupling coefficient at the saturated condition in low frequency
$\hat{Q}_{v,0}^{\text{sat}}$	C/m ³	Saturated effective excess charge density in low frequency
$\hat{Q}_{v,0}$	C/m ³	Effective excess charge density in low frequency
\hat{Q}_v^*	C/m ³	Complex effective excess charge density
CEC	C/kg	Cation exchange capacity
β_+	m ² /sV	Mobility of the counterions in the diffuse layer
β_+^{sur}	m ² /sV	Mobility of the counterions in the Stern layer
f_Q	-	Fraction of counterions in the Stern layer
C_0^{sat}	V/m	Streaming voltage coupling coefficient
C_w	mol/L	Salinity of pore water
F	-	Electrical formation factor
m	-	Cementation exponent of Archie's law
n	-	Saturation exponent of Archie's law
p_f	Pa	Pore-fluid pressure
ρ_f	kg/m ³	Mass density of fluid
ρ_s	kg/m ³	Mass density of solid
ρ_b^{sat}	kg/m ³	Saturated bulk mass density
\mathbf{u}_s	m/s	Averaging solid displacement
\mathbf{u}_f	m/s	Averaging pore-fluid displacement
\mathbf{w}	m/s	Averaging filtration displacement
k^*	m ²	Frequency-dependent permeability
k_0	-	Effective permeability in low frequency

k_0^{sat}	m^2	Saturated permeability in low frequency
ϕ	m^3/m^3	Porosity
α_{VG}	m^{-1}	Parameters of van Genuchten model
n_{VG}	-	Parameters of van Genuchten model
τ_w	-	Tortuosity
η_w	$\text{Pa}\cdot\text{s}$	Dynamic viscosity of pore-water
α	-	Biot coefficient
α^{sat}	-	Saturated Biot coefficient
T	$^{\circ}\text{C}$ or K	Temperature
ϵ_0	F/m	Vacuum permittivity
κ_w	-	Dielectric constant of water
κ_a	-	Dielectric constant of air
κ_s	-	Dielectric constant of solid phase
K_s	Pa	Bulk modulus of solid phase
G	Pa	Frame shear modulus
K_{fr}	Pa	Frame bulk modulus
K_w	Pa	Bulk modulus of water
K_a	Pa	Bulk modulus of air
K_G	Pa	Undrained bulk modulus
C	Pa	Biot modulus
M	Pa	Biot modulus

856 **Table A3.** Frequency- and saturation-dependent parameters and corresponding formulations

Parameter	Unit	Expression	References
Angular transition frequency $\omega_t(S_w)$	Hz	$\frac{\eta_w \phi S_w}{\rho_w k_0(S_w) \tau_w(S_w)}$	Revil & Mahardika, 2013; Solazzi et al., 2020
Tortuosity $\tau_w(S_w)$	-	$\phi F S_w^{1-n}$	Revil & Jougnot, 2008; Jougnot et al., 2018
Dynamic permeability $k^*(\omega, S_w)$	-	$\frac{k_0(S_w)}{1 - \frac{i\omega}{2\omega_t}}$	Revil & Mahardika, 2013
Effective water saturation $S_e(S_w)$	-	$\frac{S_w - S_{wr}}{1 - S_{wr}}$	

Quasi-static effective permeability $k_0(S_w)$	-	$k_0^{\text{sat}} S_e^{\frac{1}{2}} \left[1 - \left(1 - S_e^{\frac{1}{m_{VG}}} \right)^{m_{VG}} \right]^2$ $m_{VG} = 1 - n_{VG}^{-1}$	Mualem, 1976; van Genuchten, 1980
Specific moisture capacity $C_m(S_w)$	m^{-1}	$\frac{\alpha_{VG} m_{VG} \phi (1 - S_{wr}) S_e^{\frac{1}{m_{VG}}} \left(1 - S_e^{\frac{1}{m_{VG}}} \right)^{m_{VG}}}{1 - m_{VG}}$	Richards, 1931; van Genuchten, 1980
Frequency-dependent effective excess charge density $\hat{Q}_v^*(\omega, S_w)$	-	$\hat{Q}_{v,0}(S_w) \sqrt{1 - \frac{i\omega}{\omega_t}}$	Revil & Mahardika, 2013
Complex electrical conductivity $\sigma^*(\omega, S_w)$	S/m	$\frac{S_w^n \sigma_w}{F} + \sigma_{\text{sur}}(S_w) + i[\sigma_{\text{quad}}(S_w) - \omega \epsilon_0 \kappa(S_w)]$	Revil et al., 2015
Effective surface conductivity $\sigma_{\text{sur}}(S_w)$	S/m	$\frac{2}{3} m \frac{(F-1)}{F} S_w^{n-1} \beta_+ (1 - f_Q) \rho_s CEC$	Revil, 2013; Revil & Mahardika, 2013
Effective quadrature conductivity $\sigma_{\text{quad}}(S_w)$	S/m	$-\frac{2}{3} m \frac{(F-1)}{F} S_w^{n-1} \beta_+^{\text{sur}} f_Q \rho_s CEC$	Revil, 2013; Revil & Mahardika, 2013
Dielectric constant $\kappa(S_w)$	-	$\frac{(F-1)\kappa_s + S_w^n \kappa_w + (1 - S_w^n) \kappa_a}{F}$	Linde et al., 2006
Biot coefficient $\alpha(S_w)$	-	$\frac{S_w - S_{wr}}{1 - S_{wr}} \alpha^{\text{sat}}$	Revil & Mahardika, 2013
Mass density of fluid $\rho_f(S_w)$	kg/m^3	$S_w \rho_w + (1 - S_w) \rho_a$	
Bulk modulus of fluid K_f	Pa	$\frac{1}{\frac{S_w}{K_w} + \frac{1 - S_w}{K_a}}$	

858 **Acknowledgments**

859 Kaiyan Hu thanks the financial support of the National Natural Science Foundation of
860 China (Grant No. 42104069), and the special fund for the scientific and technological
861 development of Shenzhen guided by the central government of China (Grant No.
862 2021Szvup003). Hengxin Ren thanks the support from the National Natural Science Foundation
863 of China (Grant No. 42022027), the Guangdong Provincial Key Laboratory of Geophysical
864 High-resolution Imaging Technology (Grant No. 2022B1212010002), and the Shenzhen Science
865 and Technology Program (Grant No. KQTD20170810111725321). The authors acknowledge the
866 contributors and releasers of Broad Learning System codes (Chen & Liu, 2017) and the data set
867 used in this work (Hu et al., 2022) for making their resources publicly available. We wish to
868 thank editor Douglas Schmitt, associate editor Joel Sarout, and two anonymous reviewers for
869 their constructive comments and suggestions, which greatly helped us to improve our manuscript.

870 **Open Research**

871 The data set and the main codes for inversion related to this manuscript can be found in
872 the Hydrogeophysics Community of Zenodo (<https://doi.org/10.5281/zenodo.7820571>). The
873 subroutines of the broad learning system can be found at <https://broadlearning.ai/> (Chen & Liu,
874 2017). The used code of the peak-trough averaging algorithm is located at
875 https://datadryad.org/stash/share/xXcw75yKN0M_C_MMcqYVKQxb-qAvGjf7ICPnahRBH4Y
876 (Zheng et al., 2021).

877 **References**

- 878 Archie, G. E. (1942). The electrical resistivity log as an aid in determining some reservoir
879 characteristics. *Transactions of the American Institute of Mining, Metallurgical and Petroleum*
880 *Engineers*, 146, 54–62. <https://doi.org/10.2118/942054-G>
- 881 Biot, M. A. (1956). Theory of propagation of elastic waves in a fluid saturated porous solid: I.
882 low frequency range. *The Journal of the Acoustical Society of America*, 28(2), 168–178.
883 <https://doi.org/10.1121/1.1908241>
- 884 Biot, M. A. (1962a). Mechanics of deformation and acoustic propagation in porous media.
885 *Journal of Applied Physics*, 33, 1482-1498. <https://doi.org/10.1063/1.1728759>
- 886 Biot, M. A. (1962b). Generalized theory of acoustic propagation in porous dissipative media. *The*
887 *Journal of the Acoustical Society of America*, 34, 1254-1264. <https://doi.org/10.1121/1.1918315>

- 888 Bordes, C., Sénéchal, P., Barrière, J., Brito, D., Normandin, E., & Jougnot, D. (2015). Impact of
889 water saturation on seismoelectric transfer functions: a laboratory study of coseismic
890 phenomenon. *Geophysical Journal International*, 200(3), 1317-1335.
891 <https://doi.org/10.1093/gji/ggu464>
- 892 Butler, K. E., Russell, R. D., Kepic, A. W., & Maxwell, M. (1996). Measurement of the
893 seismoelectric response from a shallow boundary. *Geophysics*, 61, 1769–1778.
894 <https://doi.org/10.1190/1.1444093>
- 895 Butler, K. E., Fleming, S. W., & Russell, R. D. (1999). Field test for linearity of seismoelectric
896 conversions. *Canadian Journal of Exploration Geophysics*, 35, 20-23.
- 897 Butler, K. E., & Russell, R. D. (2003). Cancellation of multiple harmonic noise series in
898 geophysical records, *Geophysics*, 68, 1083-1090. <https://doi.org/10.1190/1.1581080>
- 899 Butler, K. E., Dupuis, J. C., & Kepic, A. W. (2007). Improvements in signal-to-noise in
900 seismoelectric acquisition. In Proceedings of exploration 07, Fifth Decennial International
901 Conference on Mineral Exploration (pp. 1137–1141), Toronto.
- 902 Butler, K. E., Kulesa, B., & Pugin, A. J. (2018). Multimode seismoelectric phenomena
903 generated using explosive and vibroseis sources. *Geophysical Journal International*, 213(2),
904 836-850. <https://doi.org/10.1093/gji/ggy017>
- 905 Carsel, R. F., & Parrish, R. S. (1988). Developing joint probability distributions of soil water
906 retention characteristics. *Water Resources Research*, 24(5), 755-769.
907 <https://doi.org/10.1029/WR024i005p00755>
- 908 Chen, C. P., & Liu, Z. (2017). Broad learning system: An effective and efficient incremental
909 learning system without the need for deep architecture. *IEEE Transactions on Neural Networks
910 and Learning Systems*, 29(1), 10-24. <https://doi.org/10.1109/TNNLS.2017.2716952>
- 911 Dahlquist, G., & Björck, Å. (1974). *Numerical Methods*. Englewood Cliffs N. J., Prentice-Hall.
- 912 Devi, M. S., Garambois, S., Brito, D., Dietrich, M., Poydenot, V., & Bordes, C. (2018). A novel
913 approach for seismoelectric measurements using multielectrode arrangements: II—Laboratory
914 measurements. *Geophysical Journal International*, 214(3), 1783–1799.
915 <https://doi.org/10.1093/gji/ggy251>
- 916 Du, J., Vong, C. M., & Chen, C. P. (2020). Novel efficient RNN and LSTM-like architectures:
917 Recurrent and gated broad learning systems and their applications for text classification. *IEEE
918 Transactions on Cybernetics*, 51(3), 1586-1597. <https://doi.org/10.1109/TCYB.2020.2969705>

- 919 Dukhin, S. S., & Derjaguin, B. V. (1974). Electrokinetic phenomena. In *Surface and Colloid*
 920 *Science*, (ed. E. Matijevic), 7, 322. Wiley.
- 921 Dupuis, J. C., & Butler, K. E. (2006). Vertical seismoelectric profiling in a borehole penetrating
 922 glaciofluvial sediments. *Geophysical Research Letters*, 33(16).
 923 <https://doi.org/10.1029/2006GL026385>
- 924 Dupuis, J. C., Butler, K. E., & Kepic, A. W. (2007). Seismoelectric imaging of the vadose zone
 925 of a sand aquifer. *Geophysics*, 72, A81–A85. <https://doi.org/10.1190/1.2773780>
- 926 Dzieran, L., Thorwart, M., Rabbel, W., & Ritter, O. (2019). Quantifying interface responses with
 927 seismoelectric spectral ratios. *Geophysical Journal International*, 217(1), 108–121.
 928 <https://doi.org/10.1093/gji/ggz010>
- 929 Dzieran, L., Thorwart, M., & Rabbel, W. (2020). Seismoelectric monitoring of aquifers using
 930 local seismicity—a feasibility study. *Geophysical Journal International*, 222(2), 874–892.
 931 <https://doi.org/10.1093/gji/ggaa206>
- 932 Feng, S., Ren, W., Han, M., & Chen, Y. W. (2019). Robust manifold broad learning system for
 933 large-scale noisy chaotic time series prediction: A perturbation perspective. *Neural*
 934 *Networks*, 117, 179–190. <https://doi.org/10.1016/j.neunet.2019.05.009>
- 935 Fitterman, D. V. (2015). Tools and techniques: Active-source electromagnetic methods. *Treatise*
 936 *on Geophysics (Second Edition)*, 11, 295–333. [https://doi.org/10.1016/B978-0-444-53802-](https://doi.org/10.1016/B978-0-444-53802-4.00193-7)
 937 [4.00193-7](https://doi.org/10.1016/B978-0-444-53802-4.00193-7)
- 938 Garambois, S., & Dietrich, M. (2001). Seismoelectric wave conversions in porous media: Field
 939 measurements and transfer function analysis. *Geophysics*, 66(5), 1417–1430.
 940 <https://doi.org/10.1190/1.1487087>
- 941 Garambois, S., & Dietrich, M. (2002). Full waveform numerical simulations of
 942 seismoelectromagnetic wave conversions in fluid-saturated stratified porous media. *Journal of*
 943 *Geophysical Research: Solid Earth*, 107(B7), 1–19. <https://doi.org/10.1029/2001JB000316>
- 944 Ghanbarian, B., Hunt, A. G., Ewing, R. P., & Sahimi, M. (2013). Tortuosity in porous media: a
 945 critical review. *Soil Science Society of America Journal*, 77(5), 1461–1477.
 946 <https://doi.org/10.2136/sssaj2012.0435>
- 947 Glover, P. W. J., & Jackson, M. D. (2010). Borehole electrokinetics. *The Leading Edge*, 29(6),
 948 724–728. <https://doi.org/10.1190/1.3447786>

- 949 Gong, X., Zhang, T., Chen, C. P., & Liu, Z. (2022). Research review for broad learning system:
950 algorithms, theory, and applications. *IEEE Transactions on Cybernetics*, *52*(9), 8922-8950.
951 <https://doi.org/10.1109/TCYB.2021.3061094>
- 952 Grobbe, N., & Slob, E. (2016). Seismo-electromagnetic thin-bed responses: Natural signal
953 enhancements? *Journal of Geophysical Research: Solid Earth*, *121*(4), 2460–
954 2479. <https://doi.org/10.1002/2015JB012381>
- 955 Grobbe, N., Revil, A., Zhu, Z., & Slob, E. (Eds.). (2020). *Seismoelectric exploration: Theory,*
956 *experiments, and applications* (Vol. 252). John Wiley & Sons.
- 957 Guarracino, L., & Jougnot, D. (2018). A physically based analytical model to describe effective
958 excess charge for streaming potential generation in water saturated porous media. *Journal of*
959 *Geophysical Research: Solid Earth*, *123*(1), 52-65. <https://doi.org/10.1002/2017JB014873>
- 960 Haartsen, M. W., & Pride, S. R. (1997). Electro seismic waves from point sources in layered
961 media. *Journal of Geophysical Research: Solid Earth*, *102*(B11), 24745–24769.
962 <https://doi.org/10.1029/97JB02936>
- 963 Haines, S. S., & Pride, S. R. (2006). Seismoelectric numerical modeling on a
964 grid. *Geophysics*, *71*(6), N57-N65. <https://doi.org/10.1190/1.2357789>
- 965 Hu, H., & Gao, Y. (2011). Electromagnetic field generated by a finite fault due to electrokinetic
966 effect. *Journal of Geophysical Research: Solid Earth*, *116*(B8), 1–14.
967 <https://doi.org/10.1029/2010JB007958>
- 968 Hu, K., Jougnot, D., Huang, Q., Looms, M. C., & Linde, N. (2020). Advancing quantitative
969 understanding of self- potential signatures in the critical zone through long-term monitoring.
970 *Journal of Hydrology*, *585*, 124771. <https://doi.org/10.1016/j.jhydrol.2020.124771>
- 971 Hu, K., Ren, H., Huang, Q., Zeng, L., Butler, K. E., Jougnot, D., Linde, N., & Holliger, K.
972 (2022). Dataset for "Water Table and Permeability Estimation from Multi-Channel
973 Seismoelectric Spectral Ratios" [Data set]. Zenodo. <https://doi.org/10.5281/zenodo.7820571>
- 974 Hu, K., Huang, Q., Han, P., Han, Z., Yang, Z., Luo, Q., et al. (2023). A hydrochemical study of
975 groundwater salinization in Qinzhou Bay, Guangxi, Southern China. *Earth and Space Science*,
976 *10*, e2022EA002565. <https://doi.org/10.1029/2022EA002565>
- 977 Huang, Q. (2002). One possible generation mechanism of co-seismic electric signals, *Proceeding*
978 *of the Japan Academy, Series B*, *78*(7), 173–178. <https://doi.org/10.2183/pjab.78.173>

- 979 Hunter, R. J. (1981). *Zeta Potential in Colloid Science: Principles and Applications*. Academic
980 Press.
- 981 Jackson, M. D. (2010). Multiphase electrokinetic coupling: Insights into the impact of fluid and
982 charge distribution at the pore scale from a bundle of capillary tubes model. *Journal of*
983 *Geophysical Research: Solid Earth*, 115(B7), 1-17. <https://doi.org/10.1029/2009JB007092>
- 984 Jardani, A., Revil, A., Boleve, A., Crespy, A., Dupont, J. P., Barrash, W., & Malama, B. (2007).
985 Tomography of the Darcy velocity from self-potential measurements. *Geophysical Research*
986 *Letters*, 34(24), 1-6. <https://doi.org/10.1029/2007GL031907>
- 987 Jardani, A., Revil, A., Slob, E., & Söllner, W. (2010). Stochastic joint inversion of 2D seismic
988 and seismoelectric signals in linear poroelastic materials: A numerical investigation. *Geophysics*,
989 75(1), N19–N31. <https://doi.org/10.1190/1.3279833>
- 990 Jougnot, D., Linde, N., Revil, A., & Doussan, C. (2012). Derivation of soil-specific streaming
991 potential electrical parameters from hydrodynamic characteristics of partially saturated soils.
992 *Vadose Zone Journal*, 11(1). <https://doi.org/10.2136/vzj2011.0086>
- 993 Jougnot, D., Rubino, J. G., Carbajal, M. R., Linde, N., & Holliger, K. (2013). Seismoelectric
994 effects due to mesoscopic heterogeneities. *Geophysical Research Letters*, 40(10), 2033-2037.
995 <https://doi.org/10.1002/grl.50472>
- 996 Jougnot, D., Jiménez-Martínez, J., Legendre, R., Le Borgne, T., Méheust, Y., & Linde, N.
997 (2018). Impact of small-scale saline tracer heterogeneity on electrical resistivity monitoring in
998 fully and partially saturated porous media: Insights from geoelectrical milli-fluidic
999 experiments. *Advances in Water Resources*, 113, 295-309.
1000 <https://doi.org/10.1016/j.advwatres.2018.01.014>
- 1001 Jougnot, D., Roubinet, D., Guarracino, L., & Mainault, A. (2020). Modeling streaming potential
1002 in porous and fractured media, description and benefits of the effective excess charge density
1003 approach. In *Advances in modeling and interpretation in near surface geophysics* (pp. 61-96).
1004 Springer, Cham.
- 1005 Jougnot, D., & Solazzi, S. G. (2021). Predicting the frequency-dependent effective excess charge
1006 density: A new upscaling approach for seismoelectric modeling. *Geophysics*, 86(5), WB77-
1007 WB86. <https://doi.org/10.1190/geo2020-0524.1>

- 1008 Jouniaux, L., & Zyserman, F. (2016). A review on electrokinetically induced seismo-electrics,
1009 electro-seismics, and seismo-magnetics for earth sciences. *Solid Earth*, 7(1), 249-284.
1010 <https://doi.org/10.5194/se-7-249-2016>
- 1011 Knight, R. J., & Endres, A. L. (2005). An introduction to rock physics principles for near-surface
1012 geophysics. In: Butler D. K. (Ed.), *Near Surface Geophysics, Part 1: Concepts and*
1013 *Fundamentals*. Society of Exploration Geophysicists, 13, p. 31-70.
- 1014 Linde, N., Binley, A., Tryggvason, A., Pedersen, L. B., & Revil, A. (2006). Improved
1015 hydrogeophysical characterization using joint inversion of cross-hole electrical resistance and
1016 ground-penetrating radar travelttime data. *Water Resources Research*, 42(11), W12404.
1017 <https://doi.org/10.1029/2006WR005131>
- 1018 Linde, N., Jougnot, D., Revil, A., Matthai, S. K., Arora, T., Renard, D., & Doussan, C. (2007a).
1019 Streaming current generation in two-phase flow conditions. *Geophysical Research Letter*, 34(3),
1020 L03306. <https://doi.org/10.1029/2006GL028878>
- 1021 Linde, N., Revil, A., Bolève, A., Dagès, C., Castermant, J., Suski, B., & Voltz, M. (2007b).
1022 Estimation of the water table throughout a catchment using self-potential and piezometric data in
1023 a Bayesian framework. *Journal of Hydrology*, 334, 89–99. [https://doi.org/10.](https://doi.org/10.1016/j.jhydrol.2006.09.027)
1024 [1016/j.jhydrol.2006.09.027](https://doi.org/10.1016/j.jhydrol.2006.09.027)
- 1025 Mao, S., Lecointre, A., van der Hilst, R. D., & Campillo, M. (2022). Space-time monitoring of
1026 groundwater fluctuations with passive seismic interferometry. *Nature Communications*, 13, 4643.
1027 <https://doi.org/10.1038/s41467-022-32194-3>
- 1028 Mikhailov, O. V., Haartsen, M. W., & Toksöz, M. N. (1997). Electro seismic investigation of the
1029 shallow subsurface: Field measurements and numerical modeling. *Geophysics*, 62, 97–105.
1030 <https://doi.org/10.1190/1.1444150>
- 1031 Monachesi, L. B., Zyserman, F. I., & Jouniaux, L. (2018). An analytical solution to assess the
1032 SH seismoelectric response of the vadose zone. *Geophysical Journal International*, 213(3),
1033 1999–2019. <https://doi.org/10.1093/gji/ggy101>
- 1034 Mualem, Y. (1976). A new model for predicting the hydraulic conductivity of unsaturated porous
1035 media, *Water Resources Research*, 12(3), 513–522. <https://doi.org/10.1029/WR012i003p00513>
- 1036 Niu, Q., & Zhang, C. (2019). Permeability prediction in rocksexperiencing mineral precipitation
1037 anddissolution: A numerical study. *Water Resources Research*, 55(4), 3107–3121.
1038 <https://doi.org/10.1029/2018WR024174>

- 1039 Pao, Y. H., Park, G. H. & Sobajic, D. J. (1994). Learning and generalization characteristics of
1040 the random vector functional-link net, *Neurocomputing*, 6(2), 163–180.
1041 [https://doi.org/10.1016/0925-2312\(94\)90053-1](https://doi.org/10.1016/0925-2312(94)90053-1)
- 1042 Pride, S. (1994). Governing equations for the coupled electromagnetics and acoustics of porous
1043 media. *Physical Review B*, 50(21), 15678. <https://doi.org/10.1103/PhysRevB.50.15678>
- 1044 Pride, S. R., & Haartsen, M. W. (1996). Electro seismic wave properties. *The Journal of the*
1045 *Acoustical Society of America*, 100, 1301–1315. <https://doi.org/10.1121/1.416018>
- 1046 Pride, S. R., & Garambois, S. (2002). The role of Biot slow waves in electro seismic wave
1047 phenomena. *The Journal of the Acoustical Society of America*, 111, 697–
1048 706. <https://doi.org/10.1121/1.1436066>
- 1049 Ren, H., Huang, Q., & Chen, X. (2007). Numerical simulation of seismoelectromagnetic waves
1050 in layered porous media. In *Paper Presented at Proceeding of the 8th China International Geo-*
1051 *Electromagnetic Workshop*.
- 1052 Rabbel, W., Iwanowski Strahser, K., Strahser, M., Dzieran, L., & Thorwart, M. (2020).
1053 Seismoelectric field measurements in unconsolidated sediments in comparison with other
1054 methods of near surface prospecting. In: Grobbe, N., Revil, A., Zhu, Z., & Slob, - E. (Eds.),
1055 *Seismoelectric exploration: Theory, experiments, and applications*, American Geophysical
1056 Union Monograph Vol. 252, John Wiley & Sons, p. 347-363.
- 1057 Ren, H., Huang, Q. & Chen, X. (2010). A new numerical technique for simulating the coupled
1058 seismic and electromagnetic waves in layered porous media, *Earthquake Science*, 23(2), 167–
1059 176. <https://doi.org/10.1007/s11589-009-0071-9>
- 1060 Ren, H., Huang, Q., & Chen, X. (2016a). Existence of evanescent electromagnetic waves
1061 resulting from seismoelectric conversion at a solid–porous interface. *Geophysical Journal*
1062 *International*, 204(1), 147-166. <https://doi.org/10.1093/gji/ggv400>
- 1063 Ren, H., Huang, Q., & Chen, X. (2016b). Numerical simulation of seismo-electromagnetic fields
1064 associated with a fault in a porous medium. *Geophysical Journal International*, 206, 205–220.
1065 <https://doi.org/10.1093/gji/ggw144>
- 1066 Ren, H., Huang, Q., & Chen, X. (2018). Quantitative understanding on the amplitude decay
1067 characteristic of the evanescent electromagnetic waves generated by seismoelectric
1068 conversion. *Pure and Applied Geophysics*, 175(8), 2853-2879. [https://doi.org/10.1007/s00024-](https://doi.org/10.1007/s00024-018-1823-z)
1069 [018-1823-z](https://doi.org/10.1007/s00024-018-1823-z)

- 1070 Revil, A., & Cerepi, A. (2004). Streaming potentials in two-phase flow conditions. *Geophysical*
1071 *Research Letters*, 31(11). <https://doi.org/10.1029/2004GL020140>
- 1072 Revil, A., & Linde, N. (2006). Chemico-electromechanical coupling in microporous
1073 media. *Journal of Colloid and Interface Science*, 302(2), 682-694.
1074 <https://doi.org/10.1016/j.jcis.2006.06.051>
- 1075 Revil, A., Linde, N., Cerepi, A., Jougnot, D., Matthäi, S., & Finsterle, S. (2007). Electrokinetic
1076 coupling in unsaturated porous media. *Journal of Colloid & Interface Science*, 313(1), 315-327.
1077 <https://doi.org/10.1016/j.jcis.2007.03.037>
- 1078 Revil A., & Jougnot D. (2008). Diffusion of ions in unsaturated porous materials. *Journal of*
1079 *Colloid & Interface Science*, 319(1), 226-235. <https://doi.org/10.1016/j.jcis.2007.10.041>
- 1080 Revil, A., Karaoulis, M., Johnson, T., & Kemna, A. (2012). Some low-frequency electrical
1081 methods for subsurface characterization and monitoring in hydrogeology. *Hydrogeology*
1082 *Journal*, 20(4), 617–658. <https://doi.org/10.1007/s10040-011-0819-x>
- 1083 Revil, A. (2013). Effective conductivity and permittivity of unsaturated porous materials in the
1084 frequency range 1 mHz–1GHz. *Water Resources Research*, 49(1), 306-327.
1085 <https://doi.org/10.1029/2012WR012700>
- 1086 Revil, A., & Jardani, A. (2013). *The self-potential method: Theory and applications in*
1087 *environmental geosciences*. Cambridge University Press.
- 1088 Revil, A., & Mahardika, H. (2013). Coupled hydromechanical and electromagnetic disturbances
1089 in unsaturated porous materials. *Water Resources Research*, 49(2), 744-766.
1090 <https://doi.org/10.1002/wrcr.20092>
- 1091 Revil, A., Jardani, A., Sava, P., & Haas, A. (2015). *The Seismoelectric Method: Theory and*
1092 *Applications*. John Wiley & Sons.
- 1093 Richards, L. A. (1931). Capillary conduction of liquids through porous media, *Physics*, 1, 318 –
1094 333. <https://doi.org/10.1063/1.1745010>
- 1095 Rosas-Carbajal, M., Jougnot, D., Rubino, J. G, Monachesi, L., Linde, N., & Holliger, K. (2020).
1096 Seismoelectric signals produced by mesoscopic heterogeneities: spectroscopic analysis of
1097 fractured media. In: Grobge, N., Revil, A., Zhu, Z., & Slob, - E. (Eds.), *Seismoelectric*
1098 *exploration: Theory, experiments, and applications*, American Geophysical Union Monograph
1099 Vol. 252, John Wiley & Sons, p. 269-287.

- 1100 Rutherford, S. R., & Williams, R. H. (1989). Amplitude-versus-offset variations in gas
1101 sands. *Geophysics*, *54*(6), 680-688. <https://doi.org/10.1190/1.1442696>
- 1102 Solazzi, S. G., Rubino, J. G., Jougnot, D., & Holliger, K. (2020). Dynamic permeability
1103 functions for partially saturated porous media. *Geophysical Journal International*, *221*(2), 1182-
1104 1189. <https://doi.org/10.1093/gji/ggaa068>
- 1105 Sen, P.N., & Goode, P. A. (1992). Influence of temperature on electrical conductivity on shaly
1106 sands. *Geophysics*, *57*, 89–96. <https://doi.org/10.1190/1.1443191>
- 1107 Solazzi, S. G., Bodet, L., Holliger, K., & Jougnot, D. (2021). Surface-wave dispersion in
1108 partially saturated soils: The role of capillary forces. *Journal of Geophysical Research: Solid*
1109 *Earth*, *126*, e2021JB022074. <https://doi.org/10.1029/2021JB022074>
- 1110 Solazzi, S.G., Thanh. L.D., Hu, K., & Jougnot, D. (2022). Modeling the frequency-dependent
1111 effective excess charge density in partially saturated porous media. *Journal of Geophysical*
1112 *Research: Solid Earth*, *127*(11): e2022JB024994. <https://doi.org/10.1029/2022JB024994>
- 1113 Soldi, M., Jougnot, D., & Guarracino, L. (2019). An analytical effective excess charge density
1114 model to predict the streaming potential generated by unsaturated flow. *Geophysical Journal*
1115 *International*, *216*(1), 380-394. <https://doi.org/10.1093/gji/ggy391>
- 1116 Soldi, M., Guarracino, L., & Jougnot, D. (2020). An effective excess charge model to describe
1117 hysteresis effects on streaming potential. *Journal of Hydrology*, *588*, 124949.
1118 <https://doi.org/10.1016/j.jhydrol.2020.124949>
- 1119 Thanh, L. D., Jougnot, D., Solazzi, S. G., Van Nghia, N., & Van Do, P. (2022). Dynamic
1120 streaming potential coupling coefficient in porous media with different pore size
1121 distributions. *Geophysical Journal International*, *229*(1), 720-735,
1122 <https://doi.org/10.1093/gji/ggab491>
- 1123 Thompson, A. H., & Gist, G. A. (1993). Geophysical applications of electrokinetic conversion.
1124 *The Leading Edge*, *12*, 1169–1173. <https://doi.org/10.1190/1.1436931>
- 1125 van Genuchten, M. T. (1980). A closed-form equation for predicting the hydraulic conductivity
1126 of unsaturated soils. *Soil Science Society of America Journal*, *44*(5), 892-898.
1127 <https://doi.org/10.2136/sssaj1980.03615995004400050002x>
- 1128 Wang, J., Zhu, Z., Gao, Y., Morgan, F. D., & Hu, H. (2020). Measurements of the seismoelectric
1129 responses in a synthetic porous rock. *Geophysical Journal International*, *222*(1), 436-448.
1130 <https://doi.org/10.1093/gji/ggaa174>

- 1131 Warden, S., Garambois, S., Jouniaux, L., Brito, D., Sailhac, P., & Bordes, C. (2013).
1132 Seismoelectric wave propagation numerical modelling in partially saturated
1133 materials. *Geophysical Journal International*, *194*(3), 1498-1513.
1134 <https://doi.org/10.1093/gji/ggt198>
- 1135 Wu, S., Huang, Q., & Zhao, L. (2021). Conventional neural network inversion of airborne
1136 transient electromagnetic data. *Geophysical Prospecting*, *69*(8-9), 1761-1772.
1137 <https://doi.org/10.1111/1365-2478.13136>
- 1138 Yang, X. H., Han, P., Yang, Z., Miao, M., Sun, Y. C., & Chen, X. (2022). Broad learning
1139 framework for search space design in Rayleigh wave inversion. *IEEE Transactions on*
1140 *Geoscience and Remote Sensing*, *60*, 1-17. Article no. 4512617.
1141 <https://doi.org/10.1109/TGRS.2022.3208616>
- 1142 Yang, X. H., Han, P., Yang, Z., & Chen, X. (2023). Two-stage broad learning inversion
1143 framework for shear-wave velocity estimation. *Geophysics*, *88*, WA219-WA237.
1144 <https://doi.org/10.1190/geo2022-0060.1>
- 1145 Yuan, S., Ren, H., Huang, Q., Zheng, X.-Z., & Chen, X. (2021). Refining higher modes of
1146 Rayleigh waves using seismoelectric signals excited by a weight-drop source: study from
1147 numerical simulation aspect. *Journal of Geophysical Research: Solid Earth*, *126*(5),
1148 e2020JB021336. <https://doi.org/10.1029/2020JB021336>
- 1149 Zhang, H.-M., Chen, X.-F., & Chang, S. (2001). Peak-trough averaging method and its
1150 applications to calculation of synthetic seismograms with shallow focuses. *Chinese Journal of*
1151 *Geophysics*, *44*(6), 791–799. <https://doi.org/10.1002/cjg2.201>
- 1152 Zhang, H.-M., Chen, X.-F., & Chang, S. (2003). An efficient numerical method for computing
1153 synthetic seismograms for a layered half-space with sources and receivers at close or same
1154 depths. In *Seismic motion, lithospheric structures, earthquake and volcanic sources: The Keiiti*
1155 *Aki volume* (pp. 467–486). Springer. <https://doi.org/10.1007/PL00012546>
- 1156 Zheng, X.-Z., Ren, H., Butler, K. E., Zhang, H., Sun, Y.-C., Zhang, W., et al. (2021).
1157 Seismoelectric and electroseismic modeling in stratified porous media with a shallow or ground
1158 surface source. *Journal of Geophysical Research: Solid Earth*, *126*(9), e2021JB021950.
1159 <https://doi.org/10.1029/2021JB021950>

- 1160 Zhu, Z., & Toksöz, M. N. (2013). Experimental measurements of the streaming potential and
1161 seismoelectric conversion in Berea sandstone. *Geophysical Prospecting*, *61*(3), 688-700.
1162 <https://doi.org/10.1111/j.1365-2478.2012.01110.x>
- 1163 Zyserman, F. I., Monachesi, L. B., & Jouniaux, L. (2017). Dependence of shear wave
1164 seismoelectrics on soil textures: a numerical study in the vadose zone. *Geophysical Journal*
1165 *International*, *208*(2), 918-935. <https://doi.org/10.1093/gji/ggw431>